

Using EAGLE simulations to study the effect of observational constraints on the determination of H I asymmetries in galaxies

Pooja V. Bilimogga,¹★ Kyle A. Oman,² Marc A. W. Verheijen,^{1,2,3}★ and Thijs van der Hulst¹

¹*Kapteyn Astronomical Institute, University of Groningen, Postbus 800, NL-9700 AV Groningen, the Netherlands*

²*Department of Physics, Durham University, South Road, Durham DH1 3LE, UK*

³*Institute for Computational Cosmology, Durham University, South Road, Durham DH1 3LE, UK*

Accepted 2022 April 27. Received 2022 April 27; in original form 2021 September 6

ABSTRACT

We investigate the effect of observational constraints such as signal-to-noise (S/N) ratio, resolution, and column density level on the H I morphological asymmetry (A_{mod}) and the effect of noise on the H I global profile (A_{flux}) asymmetry indices. Using mock galaxies from the EAGLE simulations, we find an optimal combination of the observational constraints that are required for a robust measurement of the A_{mod} value of a galaxy: a column density threshold of $5 \times 10^{19} \text{ cm}^{-2}$ or lower at a minimal S/N of 3 and a galaxy resolved with at least 11 beams. We also use mock galaxies to investigate the effect of noise on the A_{flux} values and conclude that a global profile with S/N greater than 6 is required to achieve a robust measurement of asymmetry. We investigate the relation between A_{mod} and A_{flux} indices and find them to be uncorrelated, which implies that A_{flux} values cannot be used to predict morphological asymmetries in galaxies.

Key words: methods: data analysis – methods: miscellaneous – galaxies: structure.

1 INTRODUCTION

Characterization of galaxies has been a fundamental part of astronomy for over a century. The morphology of many nearby galaxies have been characterized based on visual structures and features and subsequently classified into different categories. One of the earliest schemes of classification was introduced by Hubble (1926) who classified galaxies into ellipticals and spirals with further classification based on the presence of bars. This was later refined into the ‘Tuning Fork’ scheme by Sandage (1961). Schemes of classification that are in use today were developed by de Vaucouleurs (1959) van den Bergh (1960, 1976), and Elmegreen & Elmegreen (1987) among others. These schemes are an extension of the ‘tuning fork’ scheme and classify galaxies on the basis of prominent visual features such as bars, rings, the winding of spiral arms, and clumpiness of light in these arms. Physical properties of galaxies such as colour, stellar mass, and star formation rate correlate with their morphological type (Holmberg 1958; Roberts & Haynes 1994; Conselice 2006). Moreover, the morphological type of galaxies also correlates with the local environmental density (Dressler 1980, 1984). These correlations offer important clues about the underlying physics of galaxy formation.

As opposed to the visual and qualitative classification schemes, quantitative techniques have also been utilized to classify galaxies. Detailed investigations into the light profiles of elliptical galaxies was introduced by de Vaucouleurs (1948) and later generalized for other morphological types by Sérsic (1963). Light profiles of galaxies were decomposed into bulge and disc profiles by Kormendy (1977a, b) in addition to other complex features such as bars, lenses, and

inner and outer rings (Kormendy 1979). Such detailed quantitative studies were performed by de Jong (1996a, b) for spiral galaxies and by Kormendy (2009) for elliptical galaxies, taking advantage of charge-couple device (CCD) imaging.

Light structures in galaxies are also characterized using non-parametric methods. Using images from the Hubble space telescope, Schade et al. (1995) measured the degree of peculiarity in galaxies and Abraham et al. (1996) characterized asymmetry and concentration of distant galaxies to objectively classify their morphologies. Conselice (1997) characterized the asymmetry in nearby galaxies and found a correlation between the asymmetry values of the galaxies and their $B - V$ colour such that bluer galaxies are more asymmetric. Further investigation by Conselice, Bershadsky & Jangren (2000) revealed that the asymmetry–colour correlation is useful for classifying distant galaxies into different morphological types as well as identifying interacting systems. Together, concentration, asymmetry, and smoothness are collectively referred to as the CAS parameters and are the most common non-parametric methods to characterize galaxy structure (Conselice et al. 2003). Other parameters such as Gini and M20 have been used, in combination with the CAS parameters, to identify ultraluminous infrared galaxies (ULIRGs) and ongoing mergers (Abraham, van den Bergh & Nair 2003; Lotz, Primack & Madau 2004).

Various dynamical processes that act on galaxies not only distort the stellar distribution but also the distribution of gas. The kinematically cold, collisional, and often extended neutral atomic hydrogen (H I) disc in the outer parts of galaxies is fragile in nature and easily disturbed by external processes even before the stellar disc is affected. This makes H I an excellent tracer of environmental processes such as tidal interactions with neighbouring galaxies, mergers, and interactions with the surrounding gaseous medium.

* E-mail: pooja@astro.rug.nl (PVB); verheijen@astro.rug.nl (MAWV)

For instance, tidal interactions with a neighbouring galaxy can be inferred from long, trailing streams of gas (for example NGC 4111 and NGC 4026 mentioned in Verheijen & Zwaan 2001). When galaxies merge, complex H I features such as bridges and plumes of neutral gas may be seen around the merging system (references mentioned in Sancisi 1999). Gas-rich galaxies entering a dense cluster environment interact with the surrounding hot intracluster medium resulting in H I distributions offset from their stellar disc due to ram pressure (Chung et al. 2009). Clusters are also known to host galaxies with truncated H I discs, possibly due to harassment, starvation, or thermal evaporation (Warmels 1988; Moore, Lake & Katz 1998; Chung et al. 2009). Another peculiar feature that is commonly observed in galaxies is a lopsidedness in the H I distribution, the origin of which cannot always be explained as the result of an ongoing tidal interaction but may be the result of minor mergers or past tidal interactions (Sancisi et al. 2008). Peculiar features observed in H I are documented and classified in the H I rogues gallery (Hibbard et al. 2001), illustrating how the environmental impact on galaxies produces asymmetric and distorted H I distributions.

Baldwin, Lynden-Bell & Sancisi (1980) first studied the lopsided distribution of H I gas in ~ 20 nearby galaxies and proposed a pattern of elliptical orbits in which the gas moves to explain the existence of these features. Thereafter, several techniques have been used to characterize asymmetry in the spatial distribution of the H I gas. A Fourier decomposition method was applied to the column density maps of large and nearby galaxies in the Eridanus group by Angiras et al. (2006) and for the WHISP sample (van der Hulst, van Albada & Sancisi 2001) by van Eymeren et al. (2011). The CAS, Gini, and M20 indices were applied to H I maps of the WHISP sample by Holwerda et al. (2011) and Giese et al. (2016). Lelli, Verheijen & Fraternali (2014) applied a modified asymmetry index to study the structure of the H I distribution in irregular starburst galaxies. Holwerda et al. (2011) find that non-parametric methods only weakly correlate with visual classifications of galaxies in the WHISP sample. On the other hand, Giese et al. (2016) and Lelli et al. (2014) report that the asymmetry parameter is better suited in identifying galaxies with lopsided H I distributions.

Environmental effects on the gas disc of a galaxy can also be inferred by characterizing the global H I profile asymmetry through a comparison of the flux in the approaching and receding parts of the profile. Using this method, a large number of objects from the single-dish surveys can be analysed to understand the environmental effect with the caveat that a skewed global H I profile can result from either morphological or kinematic lopsidedness. Richter & Sancisi (1994) found that ~ 50 per cent of a sample of 1700 galaxies showed strong lopsidedness in their global profiles and concluded that lopsidedness in the global profile may be the rule rather than the exception. Haynes et al. (1998) investigated the global profiles of 104 isolated galaxies, of which ~ 50 per cent show lopsided global profiles. Similarly, Espada et al. (2011) studied high signal-to-noise (S/N) profiles of 166 extremely isolated galaxies and established an intrinsic asymmetry rate against which galaxies in different environments can be compared. Scott et al. (2018) studied galaxies in Abell 1367 and the Virgo cluster to find that 26 per cent and 16 per cent of galaxies have asymmetries in their global profiles. Bok et al. (2019) investigated the global profiles of ~ 350 close pairs of galaxies from the ALFALFA sample and found that asymmetries in global profiles are common in close pairs of galaxies. Asymmetries in global profiles have been studied for many large samples of galaxies from which environmental effects have been inferred. Effects of observational parameters such as noise and spectral resolution of

the profile on the asymmetries have been quantified by Watts et al. (2020), who also established a robust procedure for the comparison of profile asymmetries.

The application of an asymmetry index to H I column density maps from interferometric observations is a relatively new endeavour and our understanding of the effect of observational parameters on the measured morphological asymmetry values is limited. Giese et al. (2016) have used models of lopsided gas distributions to study how galaxy inclination, noise in the data cube, and the number of beams across a galaxy affects the measured morphological asymmetry value. However, each of these effects was studied separately. Since these aspects are not independent, a detailed investigation of their combined effect on the morphological asymmetry index is required. For this, we use mock H I data cubes of galaxies from the EAGLE simulations (Crain et al. 2015; Schaye et al. 2015) smoothed to different spatial resolutions and with a range of noise levels applied. We investigate what combination of constraints on the resolution, column density threshold, and noise is required to obtain a robust measurement of asymmetry in the column density maps of galaxies. We also investigate the relation between the global profile and the morphological asymmetry indices. If such a correlation exists, it would make it possible to infer the morphological asymmetry of unresolved galaxies based on their global profile asymmetry. This will be essential for upcoming H I surveys such as WALLABY (Koribalski et al. 2020) and MIGHTEE-HI (Jarvis et al. 2016) as well as deep H I imaging surveys such as LADUMA (Blyth et al. 2016) and CHILES (Fernández et al. 2013) in which many galaxies beyond the Local Universe will not be spatially resolved to measure their morphological asymmetry.

This paper is organized as follows: Section 2 describes the morphological and the global H I profile asymmetry indices, Section 3 describes the sample of mock galaxies from the EAGLE simulation used in this work, Section 4 discusses the effect of observational parameters such as column density threshold, resolution, and noise on the morphological asymmetry index. Section 5 describes the results of global profile asymmetry measurements for the mock sample as well as a verification of the effect of noise on the global profile asymmetry index. In Section 6, we investigate the relation between global profile and morphological asymmetry indices, and Section 7 summarizes the results of this work.

2 ASYMMETRY INDICES

2.1 Measuring morphological asymmetry

The asymmetry index (A) that measures the deviations from symmetry in the distribution of matter in a galaxy is defined as follows:

$$A = \frac{\sum_{i,j} |I(i, j) - I_{180}(i, j)|}{2 \sum_{i,j} |I(i, j)|}, \quad (1)$$

where I denotes the original image of the galaxy and I_{180} is the image rotated by 180° around a chosen centre. The asymmetry value is measured by taking a pixel-by-pixel difference between the original and rotated image, which is then summed and normalized by the total intensity in the image. The asymmetry index can have a value between 0 and 1. Due to the way the asymmetry index is defined, brighter pixels which tend to be near the centre of an image contribute more to the index than the fainter pixels in the outer regions. The influence of environmental processes is likely to disturb the extended outer parts of the H I disc.

To ensure an equal contribution of all pixels to the asymmetry index and to measure the contribution from the outer parts of an H I

disc, a modification to the index was introduced by Lelli et al. (2014). The modified asymmetry index (A_{mod}) is defined as

$$A_{\text{mod}} = \frac{1}{N} \sum_{i,j} \frac{|I(i, j) - I_{180}(i, j)|}{|I(i, j) + I_{180}(i, j)|}, \quad (2)$$

where the residuals are normalized with respect to the ‘local’ intensity as opposed to the total intensity of the pixels. Through this modification, asymmetries in the fainter outer parts can be better measured than with the classic asymmetry index.

The measured values of asymmetry are biased by the effect of noise and thus should be interpreted with caution especially when the S/N is low. To correct for the effects of noise, Conselice et al. (2000) calculate the bias in the asymmetry value from emission-free, i.e. blank, regions of an image. The corrected asymmetry values are then calculated as follows:

$$A_{\text{corrected}} = \frac{\sum_{i,j} |I(i, j) - I_{180}(i, j)|}{2 \sum_{i,j} |I(i, j)|} - \frac{\sum_{i,j} |B(i, j) - B_{180}(i, j)|}{2 \sum_{i,j} |I(i, j)|} \quad (3)$$

where B is the ‘blank’ image derived from applying the mask on to neighbouring blank regions of the image and B_{180} is the blank image rotated by 180° . Giese et al. (2016) pointed out that this bias parameter, designed for optical images, does not work well for typical H I distributions as the S/N is usually much lower and the background noise is on average zero, thus producing an overcorrection. Giese et al. (2016) introduced a measure of the S/N in the difference image and used machine learning methods to evaluate the bias in the measured asymmetry as a function of the S/N in the H I column density image as well as the S/N in the difference image. However, noise is not the only source of uncertainty in asymmetry measurements. Factors such as spatial resolution and inclination also affect the measured asymmetry value. The independent effect of these factors is studied by Giese et al. (2016) using model galaxies. When comparing asymmetry values of galaxies observed with different sensitivities, the choice of column density threshold applied to the maps also becomes important. Resolution and column density are not independent in H I data; lowering the spatial and spectral resolution of a data cube will improve the column density sensitivity. Therefore, an optimum combination of noise level, resolution and column density threshold is needed to measure and compare asymmetry values in an unbiased manner. In this work, we use the A_{mod} index to measure the asymmetry in the H I column density maps of mock galaxies.

2.2 Measuring asymmetries in the global H I profile

Asymmetries in the global profiles of galaxies are quantified by measuring the ratio of fluxes in the two halves of the emission line. The integrated flux ratio index (A_{flux}) is defined as follows:

$$A_{\text{flux}} = \frac{\int_{V_{\text{sys}}}^{V_{\text{high}}} S_\nu d\nu}{\int_{V_{\text{low}}}^{V_{\text{sys}}} S_\nu d\nu}, \quad (4)$$

where V_{low} and V_{high} are the velocities at the 20 per cent level of the peak flux density value of the spectrum and V_{sys} is the mid-point between the V_{low} and the V_{high} velocities. The flux values in the spectrum are linearly interpolated between consecutive channels. If the V_{low} and V_{high} velocities lie within a channel then a fraction of the flux is integrated in equation (4). If $A_{\text{flux}} < 1$ then the reciprocal of the ratio defined in equation (4) is considered instead. A symmetric profile will result in $A_{\text{flux}} = 1$ and deviations from symmetry in the spectrum will yield $A_{\text{flux}} > 1$.

When measuring and interpreting the asymmetry in a global profile, one should take into account the effect of noise in the observation as well as the orientation of the galaxy with respect to the observers’ line of sight. Using model global profiles, Watts et al. (2020) studied the dependence of A_{flux} values on the S/N ratios of the global profile. They found that at low S/N ratios, their sample of model galaxies shows higher rates of asymmetry. They also describe a robust method to account for the effect of noise on the A_{flux} values. Deg et al. (2020) investigated how A_{flux} values depend on the viewing angle and inclination using two snapshots of interacting galaxies. They find that despite an underlying morphologically asymmetric gas distribution, the shape of the global profile may be symmetric at certain combinations of viewing angle and inclination. Deg et al. (2020) infer that an asymmetric global profile indicates an asymmetric gas distribution, however, a symmetric global profile need not necessarily indicate symmetry in the underlying gas distribution.

3 THE MOCK GALAXY SAMPLE

To explore the optimal combination of observational parameters that allow for a robust measurement of asymmetries, these need to be varied over a large range of values. Data cubes from actual H I observations of galaxies are not suited for this exercise as the relevant parameters are observationally interlinked. By using mock H I data cubes from hydrodynamical simulations, parameters such as resolution and noise can be accurately and independently controlled. Low column density levels in spatial H I distribution and different orientations of the disc can be probed. In this work, we use mock H I data cubes of galaxies from the EAGLE simulations as the simulated galaxies better allow for the complexities of real galaxies to be seamlessly accounted for than model galaxies. Rotational velocities of galaxies, the resolution of the mock H I data cubes, and noise levels used in this work have been selected such that they resemble the interferometric observations of Ursa Major and Perseus–Pisces galaxies to be presented in our forthcoming publication.

3.1 The EAGLE simulations

The EAGLE simulations (Crain et al. 2015; Schaye et al. 2015) are a suite of cosmological simulations run with a modified GADGET-3 N -body Tree-PM smoothed particle hydrodynamics (SPH) code described in Springel (2005). The simulations follow the evolution of gas and dark matter over 29 snapshots over the redshift range $z = 0-20$, for a range of resolutions and parameters sets for the subgrid models. The various subgrid physical models implemented in EAGLE include the radiative cooling of gas (Wiersma, Schaye & Smith 2009a), reionization (Haardt & Madau 2001; Wiersma et al. 2009b), star formation (Schaye & Dalla Vecchia 2008), stellar mass-loss (Wiersma et al. 2009b), energy feedback from star formation (Dalla Vecchia & Schaye 2012), and active galactic nuclei (AGNs) feedback (Rosas-Guevara et al. 2015). In the simulations, the model parameters regulating the energy feedback from star formation and AGNs were calibrated to reproduce the observed galaxy stellar mass function (GSMF) at $z \sim 0$. Additionally, a dependence of the stellar feedback energy on the gas density was introduced to reproduce the galaxy mass–size relation at $z \sim 0.1$. A comprehensive description of these calibration procedures can be found in Crain et al. (2015). The EAGLE simulations use Λ CDM cosmological parameters consistent with the Planck 2014 results (Planck Collaboration I 2014): $\Omega_m = 0.307$, $\Omega_\Lambda = 0.693$, $\Omega_b = 0.04825$, $h = 0.6777$, and $\sigma_8 = 0.8288$.

We select our sample of galaxies from the RECAL model run of the EAGLE simulation ‘RecalL0025N0752’ (hereafter Recal25), which

is a cosmological volume of $(25 \text{ Mpc})^3$ (comoving) with 752^3 dark matter particles. The model initially has an equal number of dark matter and baryonic particles, with a dark matter particle mass of $1.21 \times 10^6 M_\odot$, and an initial baryonic particle mass of $2.26 \times 10^5 M_\odot$. In the simulation box, galaxies are defined as gravitationally bound subhaloes, which are identified using the SUBFIND algorithm (Springel 2005; Dolag et al. 2009). Initially, the dark matter particles are grouped into haloes by running the friends-of-friends (FoF) algorithm with a linking length of 0.2 times the mean interparticle separation. Gas and star particles are assigned to the same FoF halo as their nearest dark matter particle. Within an FoF halo, saddle points in the density distribution are used to define substructures. Any particles that are not bound gravitationally to the identified substructure are removed and resulting substructures are called subhaloes. In each substructure identified by the algorithm, the most massive subhalo with the lowest value of gravitational potential is defined as a ‘central galaxy’ and remaining subhaloes in the substructure are labelled as ‘satellite galaxies’. The position of a galaxy is defined by the position of the particle which has the lowest value of its gravitational potential within the subhalo (see Schaye et al. 2015, for more details).

3.2 Mock H I data cubes

We select 189 galaxies from the Recal25 simulation that are central galaxies, i.e. the most massive in their FoF group, with maximum rotational velocities (V_{max}) in the range $80 \text{ km s}^{-1} < V_{\text{max}} < 200 \text{ km s}^{-1}$ inferred from the rotation curve. We choose this range to match the V_{max} values of galaxies in the Ursa Major volume targeted with the Westerbork Synthesis Radio Telescope (WSRT) as described in table 3 of Verheijen & Sancisi (2001). This results in the sample having H I masses in the range $8.08 < \log(M_{\text{HI}}/M_\odot) < 10.25$, however, we do not enforce this in the selection of our sample. To create a mock H I cube, we use MARTINI¹ (Oman 2019) which is a modular package for the creation of synthetic resolved H I data cubes from SPH simulations of galaxies. The underlying methodology used to create mock H I datacubes is as follows (see also section 3.3 of Oman et al. 2019). Following the prescription of Rahmati et al. (2013), the neutral hydrogen gas fraction for each gas particle is calculated while accounting for self-shielding from the ionizing background radiation. Thereafter, the molecular component of the gas particle is computed using the empirical pressure-dependent relation by Blitz & Rosolowsky (2006). This empirical prescription is used so that the partitions of the atomic and molecular components of the gas particles are computed consistently with other previous works that utilize the EAGLE simulation (see Bahé et al. 2016; Marasco et al. 2016; Crain et al. 2017). The pressure-dependent fraction of the molecular component of the gas particle is computed as follows:

$$R_{\text{mol}} = \left(\frac{P}{P_0} \right)^\alpha, \quad (5)$$

where $P = n_{\text{H}} k_{\text{B}} T$ is the pressure of the gas at temperature T and $P_0/k_{\text{B}} = 4.3 \times 10^4 \text{ cm}^{-3} \text{ K}$ and $\alpha = 0.92$.

Subsequently, the C^2 smoothing kernel (Wendland 1995) is used to spatially smooth the gas particles. Along each line of sight, the 21-cm line emission is modelled with a Gaussian profile centred on the particle velocity with an adaptive broadening depending on the temperature of the particle. The Gaussian thermal velocity dispersion

of a single particle is given by

$$\sigma_{\text{T}} = \sqrt{\frac{k_{\text{B}} T_{\text{g}}}{m_{\text{p}}}}, \quad (6)$$

where σ_{T} is the temperature-dependent dispersion of the velocity profile, k_{B} is the Boltzmann’s constant, T_{g} is the gas temperature, and m_{p} is the proton mass. The typical temperature of the gas particles is about 8000 K, which results in $\sigma_{\text{T}} = 8.1 \text{ km s}^{-1}$ for each particle. The exact value of this thermal velocity dispersion of a single particle, however, does not determine the total line-of-sight velocity dispersion which is dominated by the line-of-sight velocity distribution of multiple particles. This distribution of particles has a typical dispersion of several tens of kilometers per second for the galaxies in our sample.

The H I gas is assumed to be optically thin and thus each particle contributes flux proportional to its H I mass. Thereafter, a coordinate system is adopted that is centred on the minimum of the galaxy’s gravitational potential. The orientation of the galaxy is simply that it has in the intrinsic coordinate system of the simulation, with the line of sight along the first axis (x -axis). We simulate an H I observation by placing the galaxy in the Hubble flow at a distance of 17 Mpc, which is the distance to the Ursa Major volume, thereby setting the angular scale of the mock observation to 82 parsec per arcsecond. The following steps are taken so that the mock H I data cubes are similar to the data cubes of the UMa galaxies obtained with the WSRT (see Verheijen & Sancisi 2001). A mock H I data cube is created with 512^2 pixels, a pixel size of $5 \text{ arcsec} \times 5 \text{ arcsec}$, and a channel width of 4 km s^{-1} . Thereafter, we convolve the data cubes to a Gaussian beam of $12 \text{ arcsec} \times 17 \text{ arcsec}$ and also apply a Hanning taper to set the velocity resolution to 8 km s^{-1} . The unit of the pixel values in these mock data cubes is Jy beam^{-1} . At this point no instrumental noise is added to these simulated data cubes.

Since the mock data cube for each galaxy is made from the set of particles in the FoF group, there may be contamination from the presence of satellite galaxies that belong to the same FoF group but happen to be directly in the foreground or background. We do not exclude such galaxies from the mock data cube as we endeavour to keep the process as close to real-life observational situations as possible. A 3D mask, which is guided by the rms noise in the mock data cube, is sufficient in excluding distinct foreground/background galaxies from the galaxy of interest in the centre of the data cube. For the noise-free mock data cubes of all 189 galaxies, such chance alignments have been visually inspected and data cubes with satellite galaxies in them are excluded from the analysis.

In actual observed data cubes, the column density sensitivity can be improved by smoothing the data cubes to lower angular resolutions. In preparation of future comparisons to actual observed data, the mock data cubes have been further smoothed to angular resolutions of 30, 45, 56, 98, and 120 arcsec. At the distance of 17 Mpc, these angular resolutions correspond to 1.65, 2.47, 3.70, 4.62, 8.07, and 9.89 kpc, respectively. Column density maps are created by adding the pixel values along the velocity axis to obtain a total flux in units of Jy beam^{-1} . This is then converted to column density units of cm^{-2} by using

$$N_{\text{HI}} = 1.83 \times 10^{18} \int T_{\text{b}} dv, \quad (7)$$

where T_{b} corresponds to the brightness temperature of the emission in Kelvin and dv to the channel width in km s^{-1} . The conversion from

¹<https://github.com/kyleaoman/martini>

Jy beam⁻¹ to brightness temperature T_b is given by

$$T_b = \frac{605.7}{\Theta_x \Theta_y} S_v \left(\frac{\nu_o}{\nu} \right)^2, \quad (8)$$

where Θ_x and Θ_y are major and minor axes of the Gaussian beam in arcsec, S_v is the flux density in mJy beam⁻¹, and ν_o and ν are the rest and observed frequency of the H I line emission. For a distance of 17 Mpc, $\frac{\nu_o}{\nu} \sim 1$. Global profiles are derived from the mock data cubes by spatially integrating the entire flux in each channel. Asymmetries in these global profiles are measured using equation (4) and the morphological asymmetries in the column density maps are measured using equation (2) considering only pixels above the column density thresholds of 1, 2, 5, 10, 15, 20, 45×10^{19} cm⁻² for analysis purposes.

3.3 Mock H I data cubes with added noise

To measure the effect of noise on the asymmetry values, we use the WSRT data cube of UMa galaxy UGC 6805 as the noise cube. UGC 6805 is a dwarf elliptical galaxy in the Ursa Major volume with an undetectable amount of H I gas and there is no strong continuum source present in the data cube making it suitable to be used as a noise cube representative of a real observation. We add this noise cube to the noise-free mock data cubes at 12 arcsec \times 17 arcsec resolution. Next, the noise-added mock H I data cubes are smoothed to lower angular resolutions with circular beams of 30, 45, and 56 arcsec and a velocity resolution of 20 km s⁻¹. The noise at the highest resolution is scaled such that column densities of 1, 2, 5, 10, 15, and 20×10^{19} cm⁻² have an S/N of 1, 2, 3, 4, and 5 at the different angular resolutions. This results in 120 mock H I data cubes for every galaxy selected from Recal25, each with a different combination of resolution and noise level.

Each of the 120 noise-added mock data cubes were smoothed to 98 arcsec and 40 km s⁻¹ resolution in order to define a 3D mask to isolate the H I emission. We applied a clip level of 2.5σ to create a 3D mask where pixels below the clip level are set to zero and above to one. This 3D mask is then applied to the corresponding higher resolution data cube and column density maps are created using equation (7). S/N ratios corresponding to a column density level are measured according to the method described in Verheijen & Sancisi (2001) and is briefly described here. The 3D mask is put at eight different positions in the noise-added mock data cube which are devoid of H I line emission and summing the flux along the frequency axis provides eight signal free maps. A noise map is then created by calculating for each pixel in this map the variance of the eight values of the corresponding pixels in the signal free maps. Finally, an S/N map is acquired by dividing the N_{HI} map by the noise map. For the 120 noise-added mock data cubes of each galaxy, we create a corresponding 3D mask, a column density map, and an S/N map. We also measure morphological asymmetries using equation (2) including pixels above a column density threshold under consideration.

To create global profiles with noise, we apply the same 3D mask used to create the column density map and sum the flux in each channel of the mask-applied data cube. Asymmetries in the global profile are measured using equation (4). For each channel of the profile, the uncertainty in the flux is estimated by multiplying the noise with the square root of the number of independent beams enclosed within the mask. The uncertainty in the flux varies with channel as the 3D mask has different number of pixels in each channel. We then calculate the S/N value for each channel and the S/N

value of the global profile is defined as the average of the S/N values in all the channels of the profile. Note that this is not the maximum S/N of the total flux when using the matched filter technique described in Saintonge (2007). Since we are interested in measuring profile shapes at a fixed velocity resolution, we prefer to express the S/N at a fixed velocity resolution as well.

In Appendix A, we present the properties of mock galaxies mentioned in this section along with the catalogued GroupNumber of the FoF halo in the Recal25 run of the EAGLE simulations. For each galaxy, we present noise-free column density maps at various angular resolutions and a noise-free global profile in the form of an H I atlas in Appendix B.

4 ESTIMATING BIAS IN MORPHOLOGICAL ASYMMETRY INDEX DUE TO OBSERVATIONAL CONSTRAINTS

Characterization of the asymmetry in the H I morphology of galaxies is prone to uncertainties due to various observational parameters such as angular resolution, column density threshold, and the S/N ratio of this threshold. To characterize morphological asymmetries in the outer H I disc of galaxies a low column density threshold is required and to be able to detect gas in the outer H I disc, a high sensitivity to low surface density emission is imperative. This can be achieved by degrading the angular resolution of observations or, when possible, by extending the integration period. Lowering the resolution reduces the noise in units of Kelvin and thereby improves the S/N ratio corresponding to a certain column density level in a column density map. However, the resolution should not be lowered so much that asymmetric features in H I maps of galaxies are washed out. In addition, the chosen column density threshold should be unaffected by noise to obtain a robust measure of the morphological asymmetry. In this section, we quantify the constraints on column density threshold, resolution, and S/N that are required to reliably measure the morphological asymmetry of galaxies using the A_{mod} index.

4.1 The effect of column density threshold on A_{mod}

In order to identify an acceptable low value of the column density threshold that can characterize asymmetries in the outer H I disc of galaxies, we take advantage of the noise-free column density maps derived from the EAGLE simulations, in which the column densities can be reliably traced to values as low as 1×10^{17} cm⁻². Observationally, however, this is difficult to achieve. The HALOGAS survey (Heald et al. 2011) is one of the deepest surveys of nearby galaxies and for the four galaxies in their pilot survey observed with the WSRT, an integration period of 120 h was required to reach 3σ column density sensitivity of about 1×10^{19} cm⁻². To observe gas in galaxies at column densities lower than this while still having sufficient angular resolution, we would need longer integration periods, which is difficult to achieve. Therefore, we use the column density threshold of 1×10^{19} cm⁻² as a reference threshold. We compare the A_{mod} values of the EAGLE galaxies measured at this reference threshold to the A_{mod} values at higher thresholds of 2, 5, 15, and 45×10^{19} cm⁻². We measure the A_{mod} values at the above-mentioned thresholds in column density maps at resolutions of 12 \times 17, 30, 45, 56, and 98 arcsec. Thereafter, at each resolution we calculate the Spearman correlation coefficient between the A_{mod} values at the reference threshold and the A_{mod} values at higher thresholds. The comparison of A_{mod} values along with the correlation coefficients is illustrated in Fig. 1.

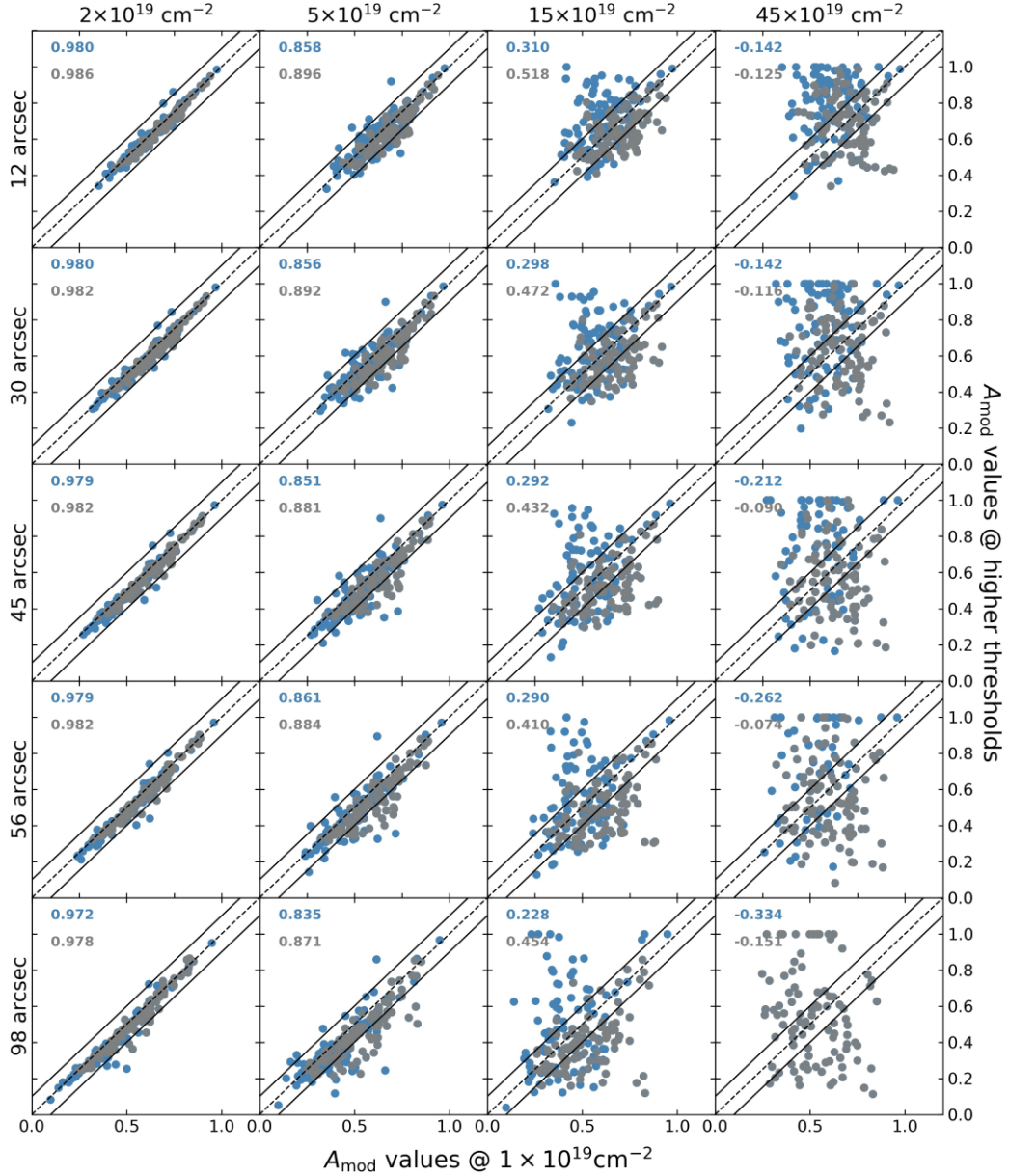


Figure 1. In this figure, asymmetries measured in noise-free mock column density maps are shown. We compare asymmetry values measured at a reference column density threshold of $1 \times 10^{19} \text{ cm}^{-2}$ to those measured at higher thresholds of 2, 5, 15, $45 \times 10^{19} \text{ cm}^{-2}$. This comparison is performed at different resolutions of the mock maps. Blue symbols indicate the asymmetry values of the whole sample while grey symbols indicate a small subset of mock galaxies that have high column density gas above $45 \times 10^{19} \text{ cm}^{-2}$ at the lowest resolution of 98 arcsec². In each panel, the numbers in the top left corner indicate the Spearman correlation coefficient between the A_{mod} values being compared and colours indicate the sample under consideration. The dashed black line indicates the line of equality and solid black lines indicate 10 per cent deviation from equality.

From Fig. 1, we find that irrespective of the angular resolution most of the galaxies that have A_{mod} values at and below a column density threshold of $5 \times 10^{19} \text{ cm}^{-2}$ are within 10 per cent of the reference A_{mod} value. This also reflects in the value of the Spearman correlation coefficients shown in Fig. 1 and thus we conclude that A_{mod} values at and below $5 \times 10^{19} \text{ cm}^{-2}$ are well correlated to the A_{mod} values at the reference threshold. Fig. 2 illustrates this as well: the correlation coefficient drops quickly when comparing A_{mod} values above $5 \times 10^{19} \text{ cm}^{-2}$. This implies that the asymmetries at the reference threshold of $1 \times 10^{19} \text{ cm}^{-2}$ are similar to asymmetries at thresholds up to $5 \times 10^{19} \text{ cm}^{-2}$. Thus, to investigate the effect of environmental processes on outer parts of H I disc of galaxies, A_{mod}

values should be measured at or below column density thresholds of $5 \times 10^{19} \text{ cm}^{-2}$. If observational limitations do not allow this and higher column density thresholds have to be applied while measuring A_{mod} then it is important to note that the A_{mod} values may not reflect the asymmetries in the outer parts of the H I disc.

Due to beam dilution, at the lowest angular resolution of 98 arcsec (or 8 kpc at the adopted distance of 17 Mpc), high column density clumps above $45 \times 10^{19} \text{ cm}^{-2}$ are not present in many of the noise-free column density maps. In our sample of 189 mock galaxies, 90 galaxies do not have gas above this threshold at 98 arcsec resolution and are therefore not shown in the bottom right panel of Fig. 1. Therefore, we define a subsample of mock galaxies for which we can

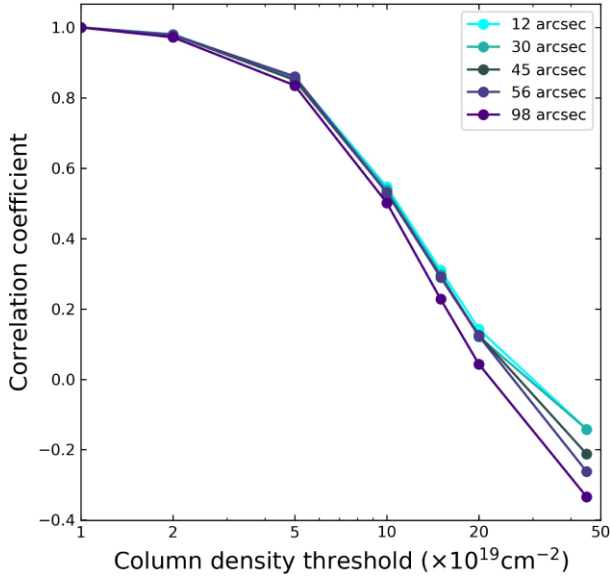


Figure 2. Correlation coefficients of the full sample are plotted as a function of the column density threshold. The coefficients correspond to those noted in the various panels of Fig. 1. Additionally, correlation coefficients at 10 and $20 \times 10^{19} \text{ cm}^{-2}$ are also included here.

measure the A_{mod} values at 98 arcsec resolution and at a threshold of $45 \times 10^{19} \text{ cm}^{-2}$. This subsample of mock galaxies is shown in grey in Fig. 1. We show the correlation coefficients of the complete mock sample as well as for the subsample in each panel of Fig. 1.

4.2 The effect of resolution on A_{mod}

In the previous subsection, we investigated the effect of changing the column density threshold on the A_{mod} values. In this subsection, we examine how changing the resolution affects the A_{mod} values. We again use noise-free column density maps of the EAGLE mock galaxies to ensure that the asymmetry values are not being affected by noise. We use column density maps at angular resolutions of 12×17 , 30, 45, 56, and 98 arcsec², and an additional resolution

of 120 arcsec^2 to further reduce the number of resolution elements across the HI map. At each angular resolution, we have measured the A_{mod} values at a column density threshold of $5 \times 10^{19} \text{ cm}^{-2}$ as this is the upper limit on the column density threshold established in Section 4.1. The column density maps of the mock galaxies above the threshold of $5 \times 10^{19} \text{ cm}^{-2}$ may be rather irregular. Therefore, we identify the minimum-sized rectangular box that encompasses all pixels above this column density threshold and calculate the number of beams that fit across the diagonal of this box.

The upper panels of Fig. 3 illustrate the distribution of the number of beams across the diagonal at different angular resolutions in the noise-free maps of the mock galaxies. At the highest resolution of $12 \text{ arcsec} \times 17 \text{ arcsec}$, all the galaxies are well resolved. As the angular resolution is lowered, the number of beams across a galaxy reduces. The lower panels of Fig. 3 illustrate the distribution of A_{mod} values of the mock galaxies at different angular resolutions. At the highest angular resolution, all the galaxies are well resolved and as the angular resolution is lowered galaxies become progressively unresolved. Similarly, the A_{mod} distribution shifts to lower asymmetry values as the resolution is lowered. At the lowest resolution, the bulk of the distribution has $A_{\text{mod}} < 0.5$ with a tail at high asymmetry values.

In an absolute sense, the number of beams across a column density map depends not only on the angular resolution of the column density map but also on the distance to the galaxy. In order to resolve nearby galaxies a large synthesized beam may be adequate, however, this may not be sufficient to resolve galaxies that are farther away. Therefore, we define resolution in terms of the number of beams across a galaxy and aim to quantify the minimum required number of beams to reliably measure A_{mod} values. Lines in the left-hand panel of Fig. 4 illustrate how A_{mod} values for an individual galaxy vary as a function of the number of beams across that galaxy. From Fig. 4, it is evident that the A_{mod} value changes little when the number of beams across a galaxy exceeds 25 while the A_{mod} value changes rapidly when the number of beams is further reduced below 25. The histogram shown at the bottom left of the left-hand panel of Fig. 4 illustrates the relative change in the A_{mod} value at 25 beams with respect to the A_{mod} value at the maximum number of beams. We find that 20 per cent of the sample shows more than 15 per cent relative change in the A_{mod} value. To quantify the change in A_{mod} with

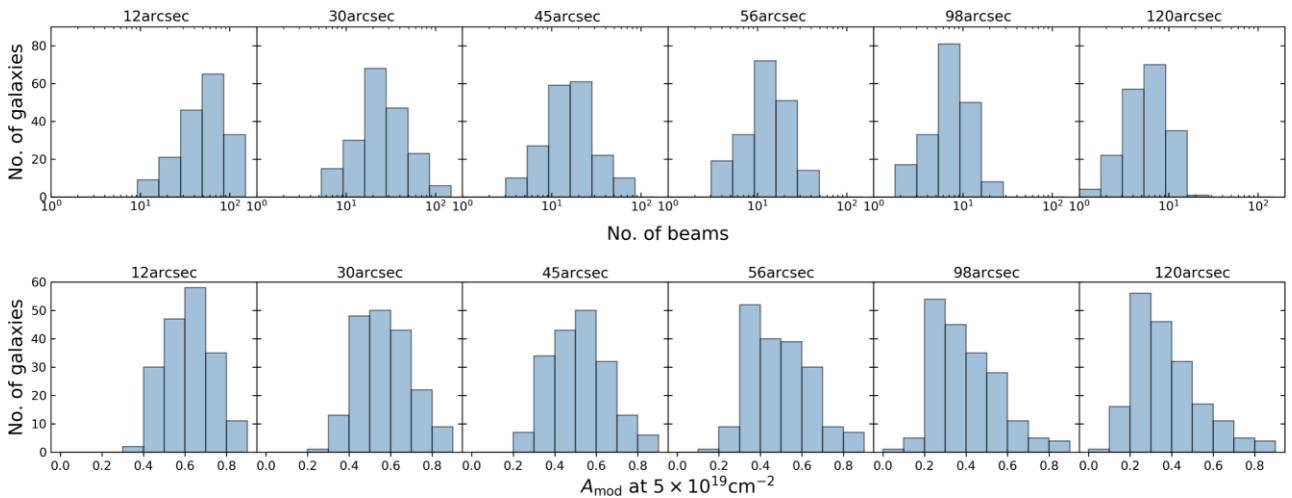


Figure 3. The top panels of this figure shows the number of beams across galaxies at different angular resolutions. The sizes are measured in noise-free column density maps of mock galaxies with a column density threshold of $5 \times 10^{19} \text{ cm}^{-2}$. The bottom panels show the asymmetry values measured in noise-free column density maps with the same threshold.

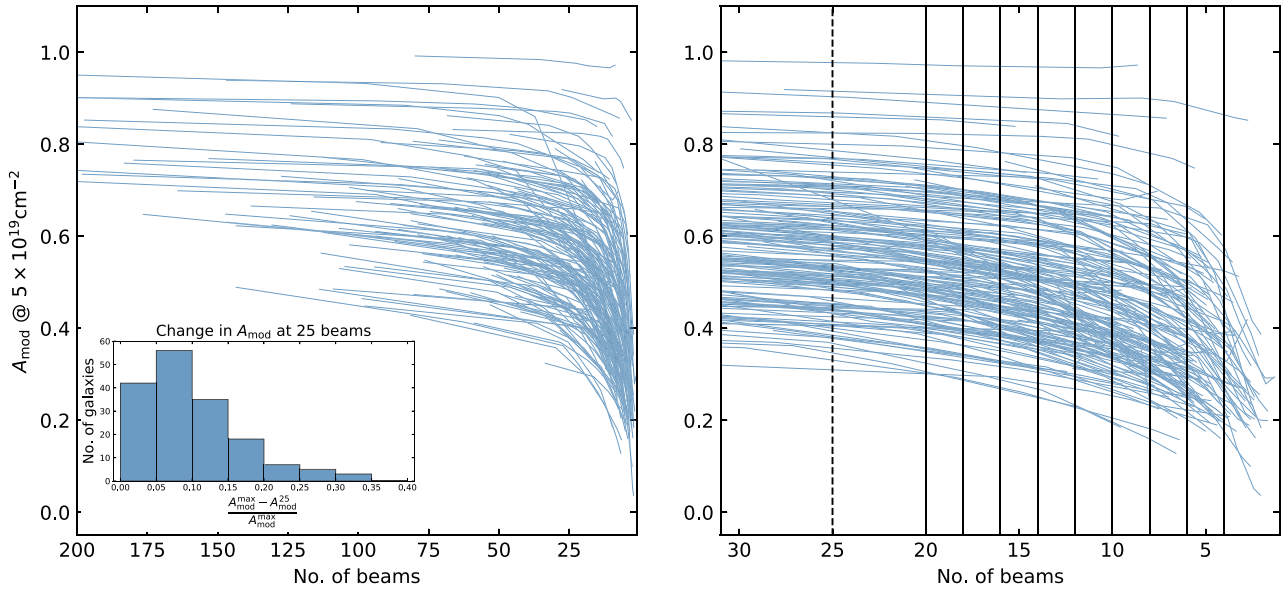


Figure 4. This figure shows how asymmetry values change as the number of beams across a galaxy is lowered. The asymmetry is measured with a threshold of $5 \times 10^{19} \text{ cm}^{-2}$. In the panel on the left, full range of sizes measured in beams is shown, while in the right-hand panel, sizes in the range of 0–30 beams are illustrated. For each galaxy in our sample, we measure the relative change in A_{mod} value at 25 beams with respect to the maximum A_{mod} value for the galaxy. The histogram of these values is shown in the left-hand panel.

resolution, we choose the A_{mod} value at 25 beams as our reference and measure the relative change in A_{mod} with respect to our reference as the number of beams across a galaxy decreases. The right-hand panel of Fig. 4 shows the variation in A_{mod} values below 25 beams in more detail while Fig. 5 shows histograms of the relative change in A_{mod} at different number of beams.

In the top right corner of each panel in Fig. 5, we indicate in black the number of galaxies that are shown in the histogram, in blue we indicate the percentage of the sample in that panel that shows more than a 30 per cent change in A_{mod} and in grey the median value of relative change in A_{mod} . For example, at 20 beams none of the galaxies in the sample have more than a 30 per cent change in A_{mod} with respect to the reference A_{mod} value at 25 beams while at 12 beams, about 6 per cent of the sample shows more than 30 per cent change in A_{mod} . From Fig. 5, we find that as the resolution reduces, a larger fraction of the sample shows more than 30 per cent change in A_{mod} . We find it acceptable to have 10 per cent of our sample showing more than 30 per cent change in A_{mod} value, which from Fig. 5 occurs at 11 beams. Therefore, we conclude that at least 11 beams across a galaxy are required to prevent a significant systematic reduction in the A_{mod} value due to resolution. We recommend the reader to choose the highest possible resolution in number of beams that their observational limitations allow for while recognizing that lowering the resolution may result in A_{mod} values that are lower than the intrinsic A_{mod} value.

4.3 Effect of signal-to-noise ratio on asymmetry

In an actual observed data cube with noise, the angular resolution, the column density threshold, and the S/N value associated with that threshold are interlinked. To investigate the minimum required S/N value that provides robust asymmetry measurements, we measure A_{mod} values of mock galaxies with and without added noise, at a threshold of $5 \times 10^{19} \text{ cm}^{-2}$ and at angular resolutions of 12×17 , 30 , 45 , 56 arcsec^2 . Additionally, we only include galaxies from the mock sample that are at least 11 beams across at the various angular

resolutions. By excluding galaxies with fewer than 11 beams across, we ensure that the change in the morphological asymmetry in the noise-added mock cubes would result solely from the addition of noise. As described in Section 3.2, noise is added to the mock data cubes such that the threshold value of $5 \times 10^{19} \text{ cm}^{-2}$ has S/N ratios of 1, 2, 3, 4, and 5. We recall that adding noise not only affects the calculation of A_{mod} but also the shape of the mask that is applied when constructing the column density map.

For every mock galaxy with added noise, we measure the relative change in A_{mod} with respect to A_{mod} measured from the noise-free column density maps as the S/N ratio varies. By implementing constraints on the column density threshold and the resolution, we aim to minimize the effect of these parameters on the measured A_{mod} values. In Fig. 6, we illustrate the relative change in A_{mod} at different S/N values for the column density threshold of $5 \times 10^{19} \text{ cm}^{-2}$ and calculate the fraction of the galaxies in the sample that show more than 30 per cent change in their A_{mod} value. This fraction is shown in the top right corner of each panel. From Fig. 6, we find that the fraction of galaxies in the sample for which A_{mod} changes more than 30 per cent reduces as the S/N increases from S/N = 1 to S/N = 5. When S/N > 3, the effect of noise on the intrinsic A_{mod} values is minimal, i.e. less than 5 per cent of the galaxies in the sample have their A_{mod} value change by more than 30 per cent. Thus, we recommend that the chosen column density threshold should have a minimum S/N of 3 to prevent a significant systematic increase in the measured A_{mod} value due to noise.

Note that galaxies that are intrinsically very asymmetric ($A_{\text{mod}} > 0.75$), the relative change in A_{mod} is small due to the fact that A_{mod} values cannot increase above 1 after the addition of noise.

5 ASYMMETRIES IN THE GLOBAL PROFILES

In the previous section, we concluded that a column density threshold of $5 \times 10^{19} \text{ cm}^{-2}$ or lower, at least 11 beams across the galaxy and an S/N of 3 or higher are required to obtain a robust estimation of A_{mod} values. In this section, we investigate the effect of adding

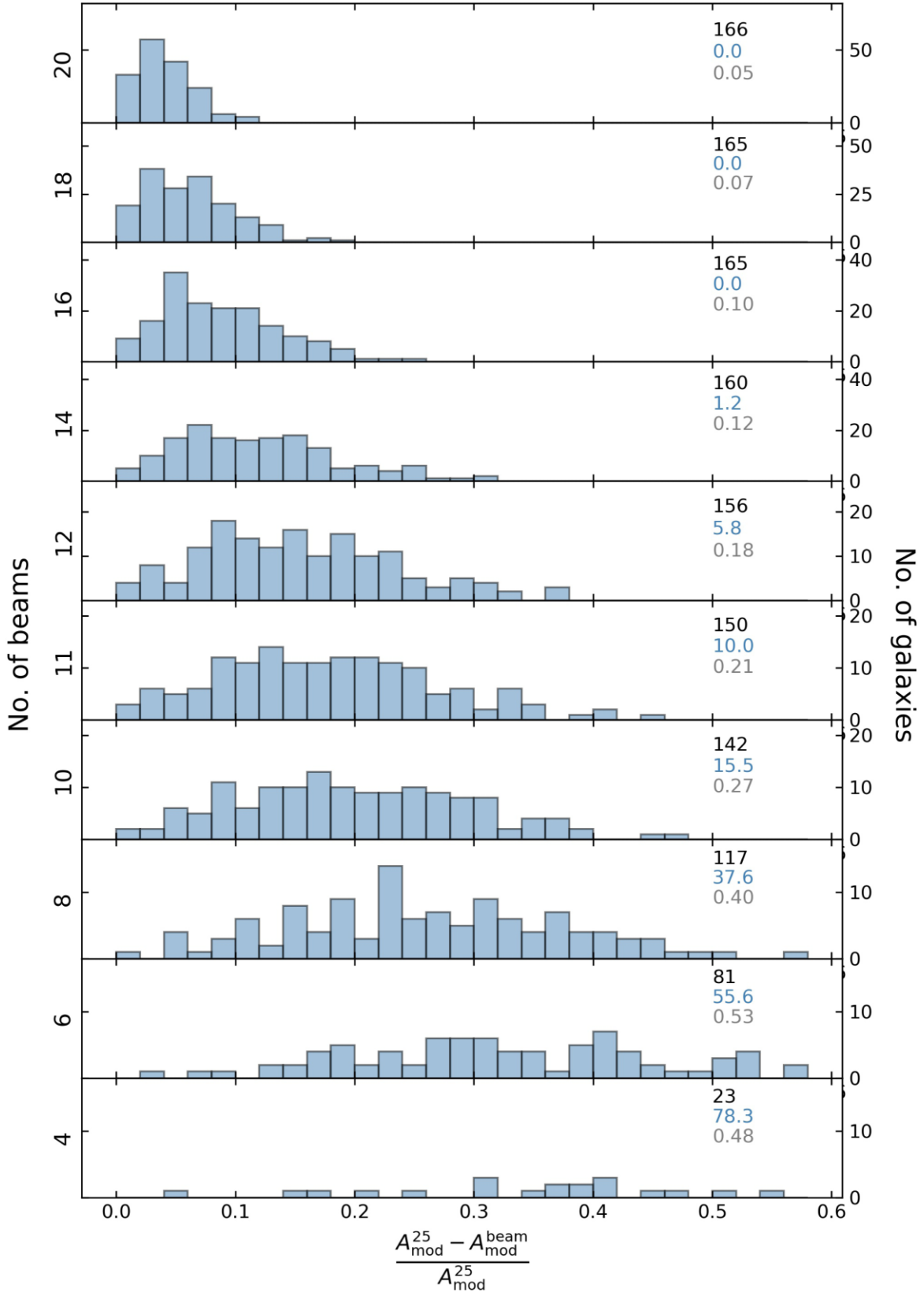


Figure 5. This figure illustrates how asymmetry values change at different number of resolution elements across a galaxy, with respect to a reference asymmetry value at 25 beams. The asymmetry values are measured at a column density threshold of $5 \times 10^{19} \text{ cm}^{-2}$. The number of galaxies in each panel is mentioned in black in the top right corner, in blue we indicate the percentage of the sample in each panel that has more than a 30 per cent change in A_{mod} values, and in grey we mention the median of the histogram in each panel.

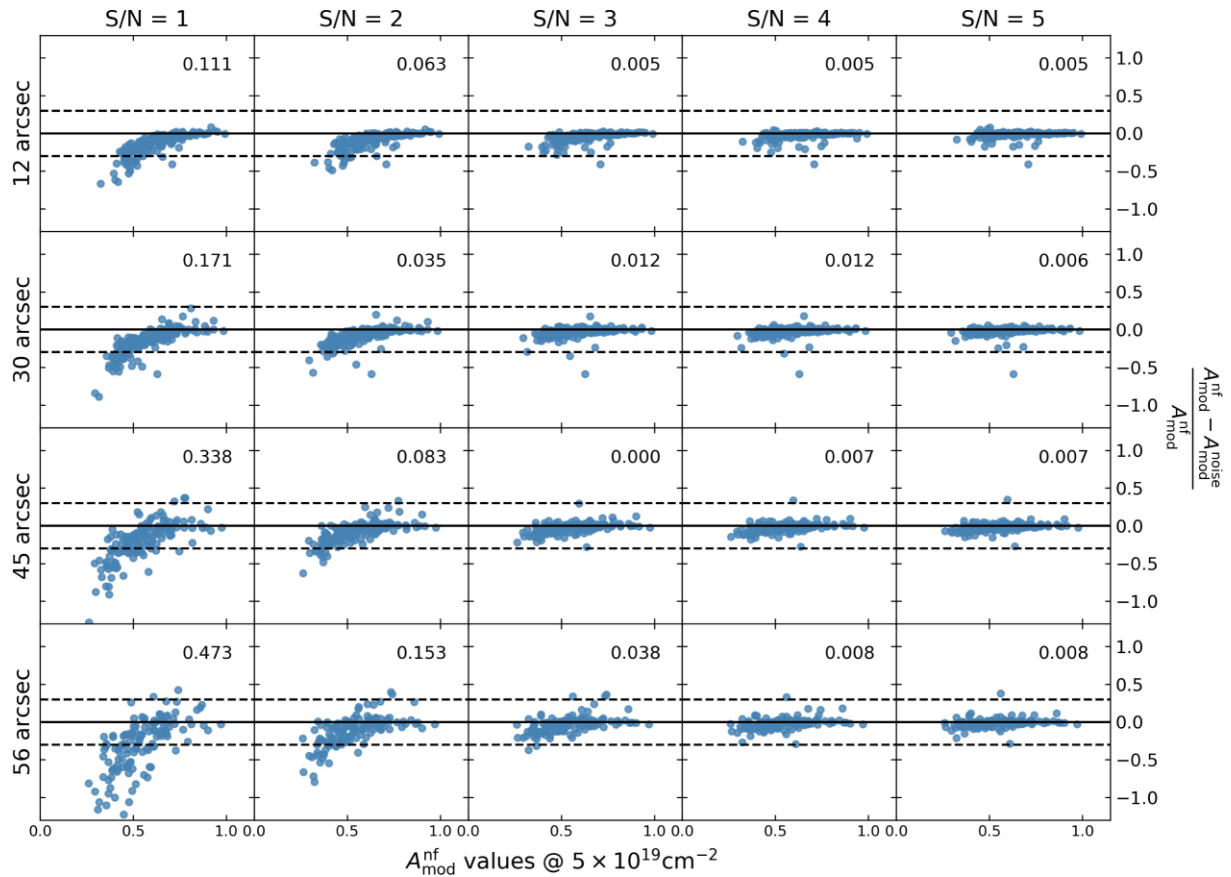


Figure 6. Relative change in asymmetry values measured at $5 \times 10^{19} \text{ cm}^{-2}$ at different S/Ns. The amount of noise added to the mock H I cubes reduces from left to right in each row as the S/N improves. In each panel, dashed black lines indicate ± 30 per cent change in asymmetry value and the numbers at the top right corner indicate the fraction of the sample with more than a 30 per cent change.

noise to the global profiles on measured A_{flux} values. For this, we use the noise-added mock datacubes described in Section 4.3 at an angular resolution of 56 arcsec^2 and a velocity resolution of 20 km s^{-1} to which we add noise such that the column density threshold of $5 \times 10^{19} \text{ cm}^{-2}$ has S/N = 3 in the integrated column density map. As described in Section 3, we create global profiles with noise by first applying a mask to the mock data cube before adding the flux in each channel. We also characterize the S/N value of the global profile by averaging the S/N in each channel. Fig. 7 shows the distribution of S/N values, indicated by the label ‘low noise’, where we find that very few galaxies have a global profile with S/N < 5. It is in global profiles with low S/N values, however, where the effect of noise on the global profile asymmetries would be evident. We therefore create another set of noise-added global profiles where we add noise to the mock data cubes such that the column density threshold of $5 \times 10^{19} \text{ cm}^{-2}$ has an S/N = 1 in the integrated column density map. In Fig. 7, we see that the S/N histogram of the second set, labelled as ‘high noise’, fills the gap in low S/N values left by the first set of global profiles. We combine the two sets of noise-added global profiles to study the effect of noise on the A_{flux} values which are further divided into roughly equal halves by splitting the sample at S/N = 5.84. The global profiles subset with S/N ≤ 5.84 is called the ‘Low S/N’ subset while that with S/N > 5.84 is called the ‘High S/N’ subset. To create noise-free global profiles, we use the mock data cubes without noise at a resolution of 56 arcsec and 20 km s^{-1} where we do not apply a 3D mask but include the flux in all the pixels in each channel of the data cube.

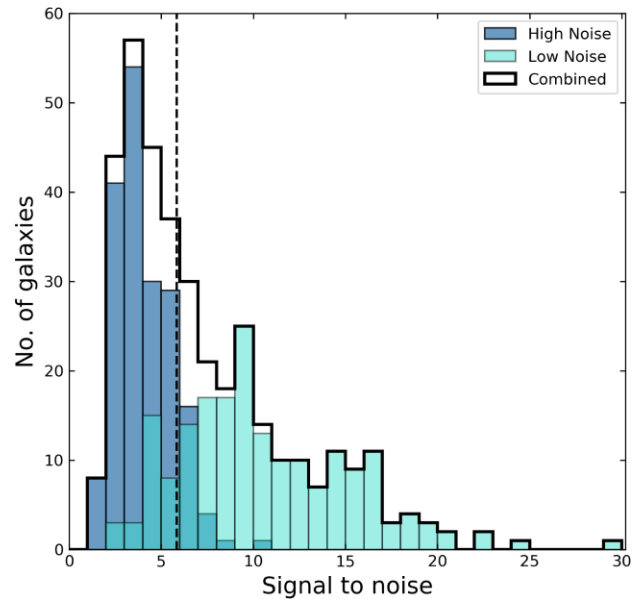


Figure 7. Distribution of S/N values of the two sets of global profiles at 56 arcsec^2 and 20 km s^{-1} . The distribution of the combined sample is also shown with a solid black line. We divide the combined sample into roughly equal halves by splitting the sample at S/N = 5.84. This S/N value is shown with a dashed black line.

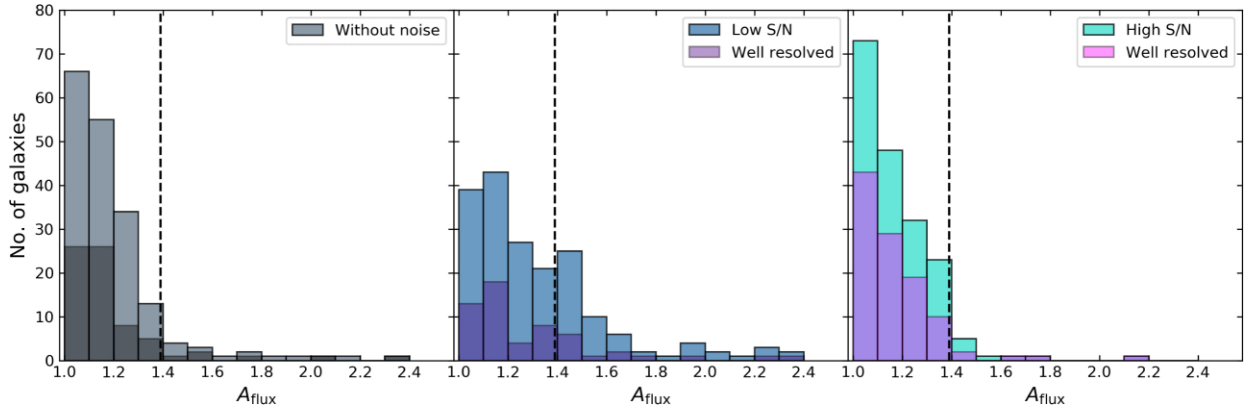


Figure 8. The left-hand panel shows the distribution of A_{flux} values without noise whereas the middle and right-hand panel show the distribution of A_{flux} for the high and low S/N subsets of noise-added global profiles. In each panel, we indicate the A_{flux} values of global profiles that have more than 10 resolution elements across the 20 per cent width. The global profiles were created from data cubes at an angular resolution of 56 arcsec^2 and velocity resolution of 20 km s^{-1} . The vertical dashed line shows the 3σ asymmetry threshold of the AMIGA sample.

In equation (4), we measure A_{flux} values in global profiles without noise and the two subsets of noise-added global profiles. We illustrate these A_{flux} values as histogram distributions in Fig. 8. Espada et al. (2011) find that the distribution of A_{flux} values of the refined AMIGA sample can be parametrized with a half-Gaussian distribution that has a $\sigma = 0.13$. This dispersion of the half-Gaussian sets an upper limit on the intrinsic dispersion of the isolated galaxies from the AMIGA sample. Espada et al. (2011) define asymmetric profiles as those having $A_{\text{flux}} > 3\sigma$ (i.e. $A_{\text{flux}} > 1.39$) and they find that 2 per cent of galaxies in their sample satisfy this criterion. Using the same criterion as that of Espada et al. (2011) as a reference, we find that 9.8 per cent of the sample has $A_{\text{flux}} > 1.39$ in global profiles without noise. In their analysis, Espada et al. (2011) use well-resolved global profiles that have more than 10 resolution elements across the 20 per cent profile width. For the sake of a fair comparison, we also measure the rate of asymmetry in global profiles with more than 10 resolution elements of the noise-free sample. We find that 9.7 per cent of the noise-free global profiles have $A_{\text{flux}} > 1.39$. This indicates that noise-free global profiles of mock galaxies are more asymmetric than the isolated galaxies described in Espada et al. (2011), which is expected because galaxies that form the mock sample are not selected from particularly isolated environments and therefore may have asymmetries due to environmental effects. In addition, the simulated galaxies may intrinsically be more asymmetric than real galaxies as shown by Bahé et al. (2016). They find that a majority of their sample has vertically disturbed H I discs. Bahé et al. (2016) also find that more than 80 per cent of their sample has H I holes larger than those seen in observed galaxies, which result from the feedback implementation in EAGLE simulations.

In global profiles of the high and low S/N subsets, we find that 7.0 per cent and 32.0 per cent of the subsets have asymmetric profiles, respectively. Considering global profiles with more than 10 resolution elements, we find that 5.6 per cent and 23.2 per cent of the high S/N and low S/N subset of the noise-added global profiles have $A_{\text{flux}} > 1.39$. Watts et al. (2020) demonstrated that an intrinsically symmetric global profile may show noise-induced asymmetries after the addition of noise, the degree of which is dependent on the S/N of the profile. They did not investigate, however, how the addition of noise affects the asymmetry of intrinsically asymmetric profiles. Yu, Ho & Wang (2020) also find that in the low S/N regime, fractional uncertainties in the A_{flux} index increases as the S/N decreases. When compared to the noise-free sample, the rate of asymmetry in the high

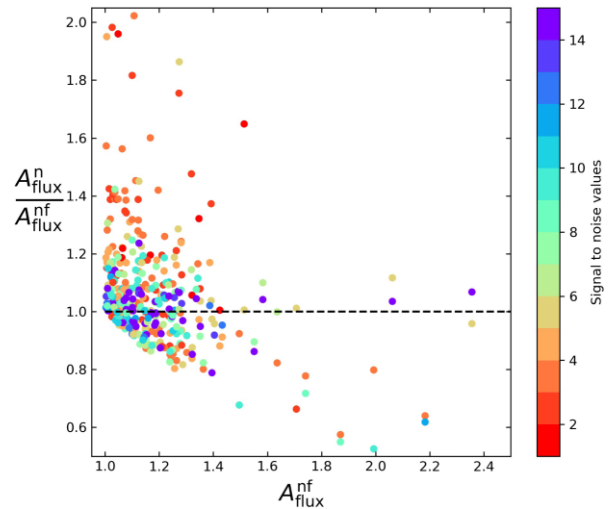


Figure 9. This figure illustrates the ratio of the noise-free A_{flux} to the noise-added A_{flux} with respect to the noise-free A_{flux} . Colours indicate the S/N of the noise-added global profile. For galaxies with a symmetric noise-free global profile, the addition of noise induces asymmetry in them, while for galaxies with intrinsically asymmetric profiles the noise-added asymmetry may increase or decrease.

S/N sample has reduced as asymmetric regions of low column density may have been excluded when the 3D mask is applied. Similarly, the rate of asymmetry in the low S/N sample has increased mainly due to the addition of noise. It should be noted, however, that choosing a fixed threshold of A_{flux} (i.e. independent of S/N) to decide the fraction of asymmetric galaxies in a sample would introduce a positive bias in the low S/N bins (Watts et al. 2020). This may be especially relevant in the low S/N subset. In the following paragraphs, we investigate in more detail the cause for the different rates of asymmetries in the high and the low S/N subsets.

To verify how the noise affects the global profile asymmetries, we examine how the ratio of the A_{flux} values in the two sets of noise-added global profiles to those without noise varies with respect to the A_{flux} values without noise. This is illustrated in Fig. 9. In this figure, the S/N value of the global profile is indicated with colours. Fig. 9 shows that for galaxies with an intrinsically symmetric global profile, the A_{flux} values increase upon addition of noise. This is similar

Table 1. Median S/N and A_{flux} ratio of galaxies in different bins of S/N values as shown in Fig. 9. We divide the sample in nine bins with 40 global profiles each, while the last bin contains 13 global profiles.

| Median S/N | Median A_{flux} ratio | 75th percentile | 25th percentile |
|------------|--------------------------------|-----------------|-----------------|
| 2.23 | 1.16 | 1.35 | 1.01 |
| 3.13 | 1.10 | 1.39 | 1.00 |
| 3.84 | 1.05 | 1.17 | 0.92 |
| 4.60 | 1.07 | 1.17 | 0.96 |
| 5.62 | 1.00 | 1.07 | 0.95 |
| 6.88 | 1.00 | 1.11 | 0.94 |
| 8.98 | 1.03 | 1.10 | 0.93 |
| 11.24 | 1.00 | 1.05 | 0.95 |
| 15.15 | 1.01 | 1.06 | 0.96 |
| 19.71 | 1.01 | 1.04 | 0.99 |

to the effect observed by Watts et al. (2020) in their model global profiles. On the other hand, for galaxies with intrinsic asymmetries in their profile, the addition of noise may increase or decrease the A_{flux} values. We divide the sample into nine bins in S/N value with 40 global profiles in each bin and an additional high S/N bin with 13 global profiles. In each bin, we measure the median S/N, the median of the ratio of the noise-added A_{flux} value to the noise-free A_{flux} value (hereafter A_{flux} ratio) as well as the 75th and 25th percentile of the A_{flux} ratio. These values are presented in Table 1 and Fig. 9, from which we conclude that global profiles with $S/N < 5.68$ have a high median A_{flux} ratio as well as a large spread in their interquartile range of the A_{flux} ratio. This indicates that the noise-added A_{flux} values with $S/N < 5.68$ are not representative of the actual noise-free A_{flux} as the added noise most often increases the asymmetries in the global profiles but could occasionally decrease the asymmetry as well. Therefore, we recommend that global profiles with $S/N > 5.5$, which is the lower bound of the $S/N = 5.68$ bin, for robust measurement of global profile asymmetries.

The addition of noise varies the shape of the global profile and thereby may increase or decrease its A_{flux} value. To have a better understanding of the effect of noise, we consider the noise-free global profile, the noise-added global profile, and additionally a mask-applied noise-free global profile where the same 3D mask is applied as in the case with noise at different S/N values. In Fig. 10, we illustrate these three versions of global profiles for three representative mock galaxies. The noise-added global profile of the mock galaxy ‘Recal25.61’ has a low S/N (2.46) and its shape is significantly different from the shape of the noise-free global profile. It is also evident that several noise peaks appear in different channels of the noise-added global profile, which are absent in the noise-free profile. However, ratio of the noise-added A_{flux} value to the noise-free A_{flux} value is still close to unity. In an actual observation, it would be difficult to determine whether the multiple peak structure in the noise-added global profile of ‘Recal25.61’ has an astrophysical origin. The mask-applied noise-free global profile also differs from the noise-free case. This implies that the mask does not enclose all regions of H I emission in the mock data cube. After the addition of noise, a part of the low surface brightness H I gas could lie below the threshold applied during creation of the mask, which then results in an underestimation of flux in the global profile as well as changing its shape.

For the other two galaxies, ‘Recal25.179’ and ‘Recal25.46’, the shapes of the noise-free global profile, noise-added global profile and the mask-applied noise-free global profile are similar but not identical. This indicates that the 3D mask encloses most of the regions of H I emission within the mock data cube. Similarly, contribution of noise to the flux in each channel is present but is

much less evident for ‘Recal25.46’ due to the high S/N of the global profile than for ‘Recal25.179’. From the behaviour of the A_{flux} ratio in different S/N bins and the effect of noise on the shape of the noise-added global profile, we conclude that a minimum S/N of 5.5 is required for robust measurements of the A_{flux} value. In global profiles with a lower S/N value, there may be a pronounced change in the shape of the global profile in addition to uncertainties in the A_{flux} measurement due to noise.

6 CORRELATION BETWEEN GLOBAL PROFILE AND MORPHOLOGICAL ASYMMETRY INDICES

Ongoing and upcoming H I imaging surveys, such as APERTIF Medium-Deep Survey,² MIGHTEE-HI (Jarvis et al. 2016), WAL-LABY (Koribalski et al. 2020), LADUMA (Blyth et al. 2016), and CHILES (Fernández et al. 2013), will have sufficient sensitivity to probe low column density gas down to $5 \times 10^{19} \text{ cm}^{-2}$ or less. However, many of the galaxies detected in these surveys beyond the Local Universe would not be sufficiently resolved to quantify morphological asymmetry and we would have to rely on the global H I profile of the galaxies alone. If a relation between the A_{mod} and A_{flux} indices exists, a morphological asymmetry may be inferred for spatially unresolved galaxies at higher redshifts.

In Fig. 11, we illustrate the comparison between the A_{mod} and the A_{flux} values. In this figure, points are coloured by the V_{max} of the galaxies, which closely traces the dynamical mass of the galaxy, while the sizes represent the number of beams across the galaxy. In the left-hand panel, we measure the A_{mod} and the A_{flux} values in noise-free mock data cubes at an angular resolution of 56 arcsec² (4.8 kpc at a distance of 17.1 Mpc) and a velocity resolution of 20 km s^{-1} . In the panel on right, we compare the A_{mod} and the A_{flux} values in noise-added mock data cubes of the ‘low noise’ sample (discussed in Section 5) at the same resolution. Additionally, we only include galaxies that are more than 11 beams resolved and have a global profile $S/N > 6$. The A_{mod} values were calculated using a column density threshold of $5 \times 10^{19} \text{ cm}^{-2}$. From Fig. 11, we find that galaxies with $A_{\text{flux}} < 1.6$ may have a wide range of A_{mod} values, some even as high as $A_{\text{mod}} = 0.9$, while all galaxies with $A_{\text{flux}} > 1.6$ tend to have $A_{\text{mod}} > 0.6$. An inspection of the mock atlas pages and data cubes reveals that these galaxies with high A_{flux} as well as A_{mod} values seem to be undergoing a merger event where the gas has not yet settled into a regularly rotating disc.

In Fig. 11, the Spearman correlation coefficient between the noise-free A_{mod} and A_{flux} is 0.19, implying that there is no significant relation between the two asymmetry indices. Similarly the correlation coefficient is 0.24 in the case of noise-added A_{mod} and A_{flux} . Our results are in conflict with the conclusions of Reynolds et al. (2020), who find a moderate correlation of ~ 0.4 between the A_{flux} and the asymmetry index A (see equation 1 values of the LVHIS, VIVA, and HALOGAS galaxies). As Reynolds et al. (2020) use the Pearson correlation coefficient and the A_{flux} values of their sample do not exceed 1.6, we use a subset of our sample with $A_{\text{flux}} < 1.6$ and measure the Pearson correlation coefficient between the A_{mod} and A_{flux} indices for this subset. We find a correlation coefficient of 0.16 and 0.19 for the noise-free and noise-added asymmetry values, which is still below the values mentioned by Reynolds et al. (2020). There may be systematic biases (due to the effects described in Section 4) in the A values mentioned by Reynolds et al. (2020) as the column

²<https://www.astron.nl/telescopes/wsrpt-apertif/>

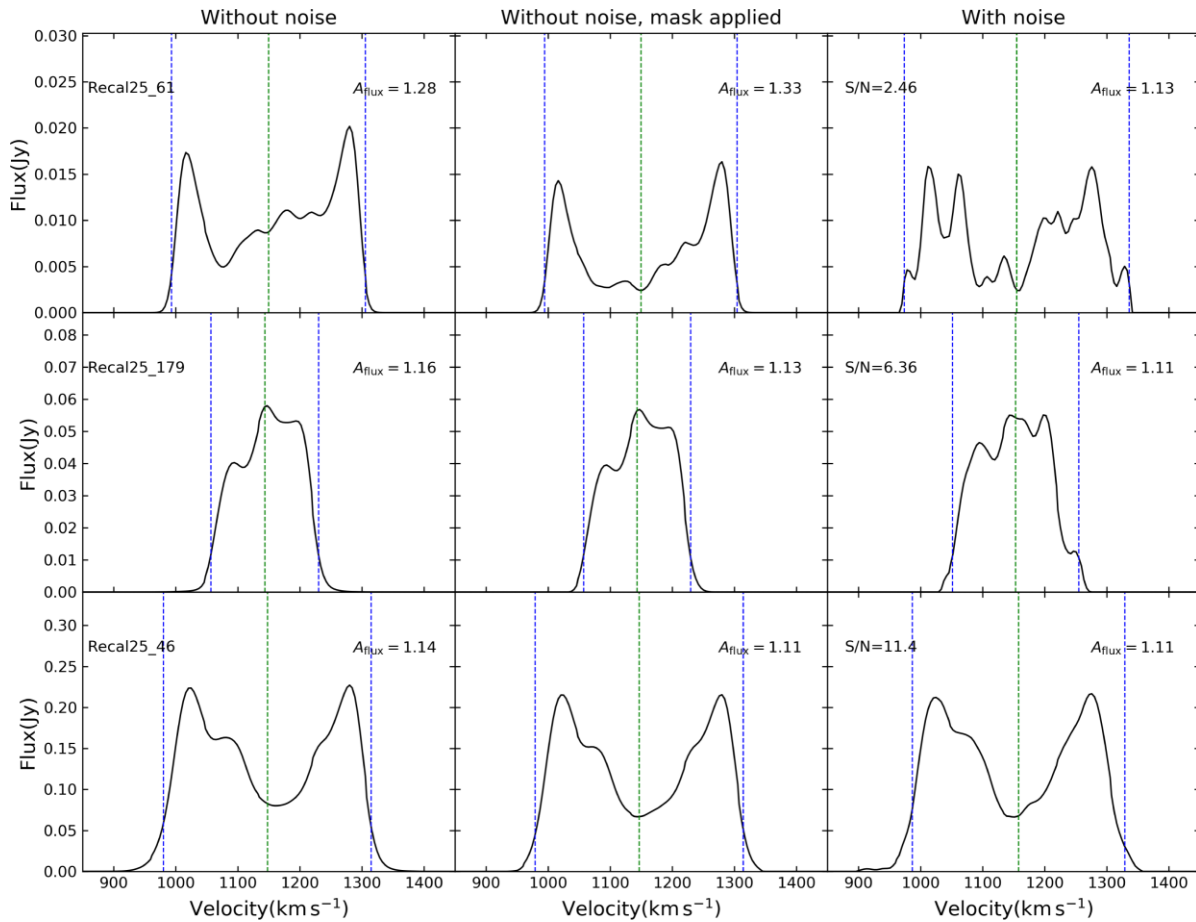


Figure 10. This figure illustrates how noise affects the shape of global profile of mock galaxies at different S/N values. In each panel, the blue dashed lines indicate velocities at 20 per cent of peak flux; the dashed green line indicates the systemic velocity of the global profile. Each row shows noise-free global profile (left-hand panel), mask-applied noise-free global profile (middle panel), and noise-added global profile (right-hand panel) of a mock galaxy. The name of the mock galaxy is shown in the left-hand panel at the top left corner. The S/N value for the global profile after the addition of noise is shown in the right-hand panel at the top left corner. The A_{flux} value for each version of the global profile is shown at the top right corner of each panel.

density threshold and the resolution at which these asymmetry values are measured are not mentioned. It is therefore hard to explain why they find a moderate correlation.

As mentioned before in Section 2.2, one reason for the lack of correlation observed in Fig. 11 could be that the orientation of the galaxy with respect to the observer may result in lower A_{flux} values even when the underlying HI distribution is asymmetric. Deg et al. (2020) find that when the inclination is greater than 20° , A_{flux} values are relatively stable against a change in inclination. However, A_{flux} values have a strong dependence on the position angle of the asymmetric feature in the galaxy. This is because both the HI distribution and the kinematics of a galaxy determine the shape of the global profile. Therefore, asymmetries in the kinematics of a galaxy could also affect the A_{flux} value. For example, Swaters et al. (1999) study two kinematically lopsided galaxies, DDO 9 and NGC 4395, with fairly symmetric HI distributions. For both DDO 9 and NGC 4395, the rotation curve on the approaching side rises and then flattens while the rotation curve on the receding side continues to rise (see figs 1 and 2 in Swaters et al. 1999). This introduces an asymmetry in the global profile despite the symmetric HI distribution. The findings of Deg et al. (2020) and Swaters et al. (1999) suggest that even if a 2D kinematic asymmetry index is considered, we may also not find a relation between the A_{flux} and the kinematic asymmetry index. Perhaps a 3D asymmetry index that captures both the kinematic and

the morphological asymmetries may have stronger correlation with the A_{flux} index.

We also examined the dependence of A_{flux} and A_{mod} values on the V_{max} and number of beams across the major axis. We expected galaxies with higher V_{max} , which are also large galaxies, to have lower A_{mod} values as these galaxies have a deeper potential and thus the gas would be more difficult to disturb. In Fig. 12, we show the histogram of A_{mod} values measured in different bins of V_{max} . The first three panels of Fig. 12, which correspond to the lowest three V_{max} bins in Fig. 11, have similar median values. However, galaxies with $V_{\text{max}} > 140 \text{ km s}^{-1}$ have a higher median A_{mod} value, while the overall distribution has also shifted to higher A_{mod} values. Bahé et al. (2016) show that EAGLE galaxies with $\log(M_{\text{HI}}/M_{\odot}) > 9.5$ have large HI holes in them that result from the feedback recipes in EAGLE. Galaxies with $V_{\text{max}} > 140 \text{ km s}^{-1}$ have a higher median HI mass which may result in them having large HI holes and consequently higher asymmetry values.

7 SUMMARY AND OUTLOOK

In this work, we have studied the effect of observational limitations on global profile and morphological asymmetry indices. For this, we used 189 mock HI data cubes of galaxies from the EAGLE

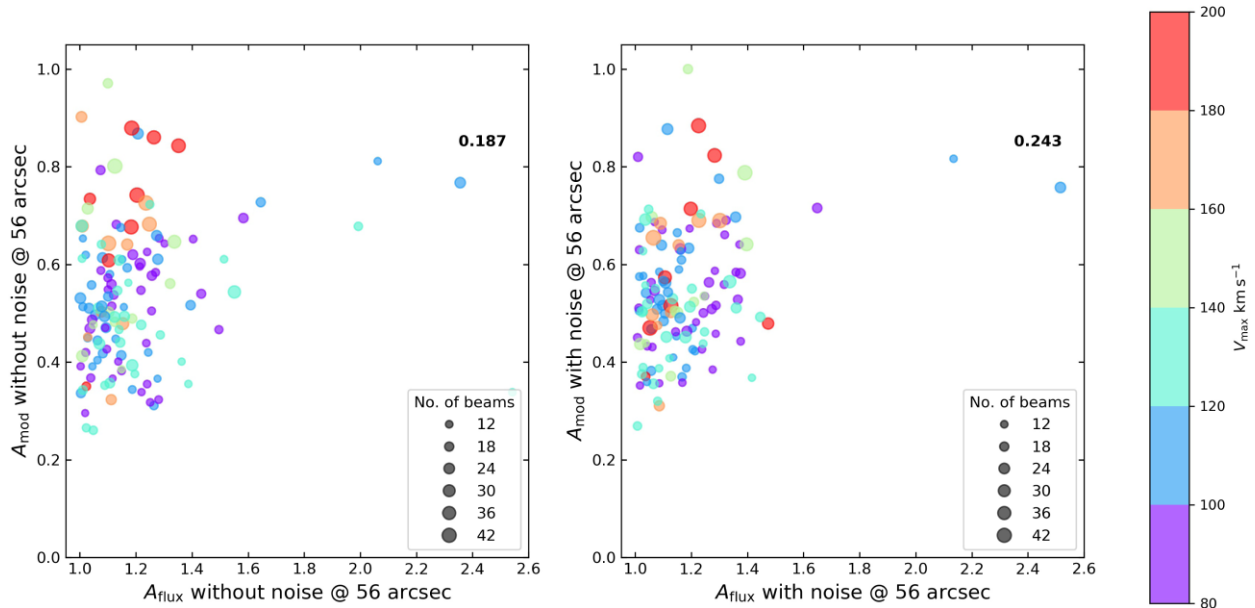


Figure 11. This figure compares asymmetry measured with different indices for the noise-free and noise-added data cubes of mock galaxies. The colours indicate the maximum rotational velocity of galaxies and the size indicates the number of beams across the diagonal of the minimum box of galaxies. The A_{flux} and A_{mod} values are measured at an angular resolution of 56 arcsec and velocity resolution of 20 km s^{-1} . The left-hand and the right-hand panel show the comparison between the noise-free and noise-added asymmetry values, respectively. The A_{mod} values are measured with a column density threshold of $5 \times 10^{19} \text{ cm}^{-2}$. The Spearman correlation coefficient between the indices is shown at the top right corner of both panels.

hydrodynamical simulations at different angular resolutions and with varied noise levels.

To quantify the morphological asymmetry of mock galaxies, we used the modified asymmetry parameter A_{mod} . We analysed column density maps with and without noise, at different resolutions, and with different column density thresholds in which we measured the asymmetries in the outer H I disc of mock galaxies. To detect signatures of environmental processes acting on galaxies, adequate sensitivity to low column densities is required. We found that the correlation between A_{mod} values at a reference column density threshold of $1 \times 10^{19} \text{ cm}^{-2}$ to those at higher column density threshold reduced as the applied column density threshold was increased (see Figs 1 and 2). Above a threshold of $5 \times 10^{19} \text{ cm}^{-2}$, the value of the correlation coefficient in Fig. 2 falls below 0.5. Therefore, a column density threshold up to $5 \times 10^{19} \text{ cm}^{-2}$ is optimal to measure asymmetries in the outer parts of H I disc that are susceptible to environmental processes. At thresholds greater than $5 \times 10^{19} \text{ cm}^{-2}$, asymmetries may result from secular evolution processes and thus may be completely unrelated to environmental influence.

Giese et al. (2016) and Lelli et al. (2014) have shown that lowering the angular resolution of a galaxy lowers its measured asymmetry value. Considering the number of beams across the minimum box of a galaxy as a metric, we found that the variation in A_{mod} values is negligible when a galaxy is resolved by more than 25 beams (see Fig. 4). With this as the reference, we measured the relative change in the A_{mod} value at fewer than 25 beams across (see Fig. 5). At 11 beams across the galaxy, only 10 per cent of the mock galaxies show more than 30 per cent relative change in their A_{mod} values. Therefore, to measure A_{mod} values that are only marginally affected by resolution, at least 11 beams across the galaxy are required.

The measured morphological asymmetry value of a galaxy generally increases with the addition of noise. To measure A_{mod} values that are relatively unaffected by noise, it is necessary to include

pixels in column density maps that have a sufficiently high S/N ratio. We considered column density maps with varying amounts of noise such that the previously motivated threshold of $5 \times 10^{19} \text{ cm}^{-2}$ has different S/N values and measured A_{mod} values with this threshold. Comparing the noise-free A_{mod} values of mock galaxies to the noise-added A_{mod} values we found that at $\text{S/N} > 3$, less than 5 per cent of the mock sample shows more than 30 per cent change in the asymmetry value (see Fig. 6). Therefore, for A_{mod} values to be minimally affected by noise, the chosen threshold should have an S/N of at least 3.

In order to ensure a fair comparison of the A_{mod} values among galaxies observed with different resolutions and sensitivities, it is important to uniformly apply the above mentioned constraints. Observational limitations that affect the modified asymmetry index A_{mod} would similarly affect the asymmetry index A as demonstrated by Giese et al. (2016). Notably, such precautions concerning the measurement of the A values for the WHISP galaxies were not taken by Holwerda et al. (2011) and were shown by Giese et al. (2016) to be unreliable. Similarly, Reynolds et al. (2020) compared the A values of LVHIS, VIVA, and HALOGAS galaxies but did not mention details regarding resolution, noise levels, and applied column density threshold. It is conceivable that the A values mentioned in Reynolds et al. (2020) are subject to biases similar to those in Holwerda et al. (2011).

The morphological asymmetry index A_{mod} can identify asymmetric galaxies. However, to identify the underlying physical processes causing these asymmetric features a combination of other non-parametric indices can be used. Bignone et al. (2017) used Gini and M20 indices to identify galaxies undergoing mergers using optical images of galaxies in the ILLUSTRIS simulation. Similarly, a combination of different non-parametric indices can be applied to the H I disc of galaxies in simulations to identify mergers, tidal interactions, and ram pressure stripping in galaxies. This will be the subject of a forthcoming study.

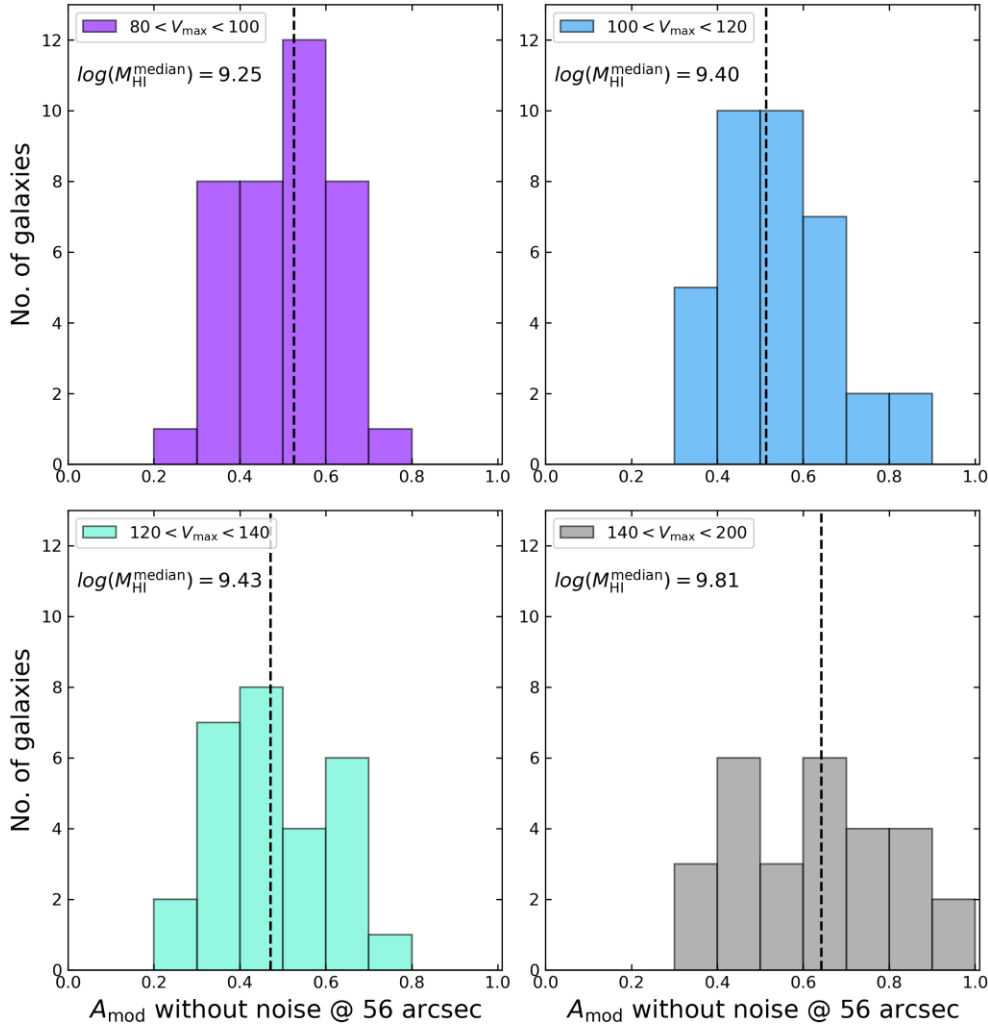


Figure 12. This figure shows the distribution of noise-free A_{mod} values of the mock galaxies in different bins of V_{max} . The first three bins in V_{max} are the same as those shown in Fig. 11, while the last three bins are combined into one as each bin has low number of galaxies. The median H I mass of the mock galaxies is shown in the upper left corner of each panel. The dashed black line in each panel indicates the median of the A_{mod} distribution. The A_{mod} values shown here are measured at 56 arcsec resolution and at a column density threshold of $5 \times 10^{19} \text{ cm}^{-2}$.

We characterize asymmetries in the global profiles of mock galaxies by measuring the A_{flux} index. We use the A_{flux} distribution of the AMIGA sample of isolated galaxies as a reference and we find that 9.8 per cent of the mock galaxies have $A_{\text{flux}} > 1.39$ when measured without noise. For the two sets of noise-added global profiles, we find that 7 per cent and 32 per cent of mock global profiles have $A_{\text{flux}} > 1.39$ in the ‘high S/N’ and ‘low S/N’ subsets, respectively. This implies that the mock galaxies from EAGLE simulations are intrinsically more asymmetric than the AMIGA sample. In global profiles with $S/N < 5.68$, the addition of noise may result in a large change in A_{flux} as compared to the noise-free A_{flux} value (see Fig. 9 and Table 1). Similarly, the shape of the global profile may also change substantially, which may or may not affect the A_{flux} measurements (see Fig. 10).

We investigate the relation between the A_{flux} and A_{mod} indices using mock data cubes and find a small correlation coefficient of ~ 0.2 for both the noise-free and noise-added asymmetry values (see Fig. 11). This lack of correlation could result from the effect of the kinematics of a galaxy on the shape of the global profile. The absence of a relation between the two asymmetry parameters implies that a

morphological asymmetry cannot be inferred from the global profile asymmetry value of spatially unresolved galaxies.

As a next step, the constraints for calculating the morphological asymmetry index derived in this work will be applied to observations of real galaxies from H I imaging surveys of the Ursa Major and the Perseus–Pisces volumes. By quantifying morphological asymmetries in the H I disc of galaxies, we will investigate the effects of environmental processes prevalent in these volumes. fig

ACKNOWLEDGEMENTS

We would like to thank the reviewer for their careful consideration of our manuscript. Their suggestions have helped improve the text greatly. PB acknowledges the Leids Kerkhoven-Bosscha Fonds for financial travel support. KAO acknowledges support by the European Research Council (ERC) through Advanced Investigator grant to C.S.Frenk, DMIDAS (GA 786910) and by the Netherlands Foundation for Scientific Research (NWO) through VICI grant 016.130.338 to MV. PB and MV acknowledge support by the Netherlands Foundation for Scientific Research (NWO) through

VICI grant 016.130.338. JMvdH acknowledges support from the European Research Council under the European Union's Seventh Framework Programme (FP/2007-2013) / ERC Grant Agreement nr. 291531 (HISTORYNU). We acknowledge the Virgo Consortium for making their simulation data available. The EAGLE simulations were performed using the DiRAC-2 facility at Durham, managed by the Institute for Computational Cosmology, and the PRACE facility Curie based in France at TGCC, CEA, Bruyères-le-Châtel. This work used the DiRAC@Durham facility managed by the Institute for Computational Cosmology on behalf of the STFC DiRAC HPC Facility (www.dirac.ac.uk). The equipment was funded by BEIS capital funding via STFC capital grants ST/K00042X/1, ST/P002293/1, ST/R002371/1, and ST/S002502/1, Durham University and STFC operations grant ST/R000832/1. DiRAC is part of the National e-Infrastructure.

DATA AVAILABILITY

The data underlying this article will be shared on reasonable request to the corresponding author.

REFERENCES

- Abraham R. G., van den Bergh S., Glazebrook K., Ellis R. S., Santiago B. X., Surma P., Griffiths R. E., 1996, *ApJS*, 107, 1
- Abraham R. G., van den Bergh S., Nair P., 2003, *ApJ*, 588, 218
- Angiras R. A., Jog C. J., Omar A., Dwarakanath K. S., 2006, *MNRAS*, 369, 1849
- Bahé Y. M. et al., 2016, *MNRAS*, 456, 1115
- Baldwin J. E., Lynden-Bell D., Sancisi R., 1980, *MNRAS*, 193, 313
- Bignone L. A., Tissera P. B., Sillero E., Pedrosa S. E., Pellizza L. J., Lambas D. G., 2017, *MNRAS*, 465, 1106
- Blitz L., Rosolowsky E., 2006, *ApJ*, 650, 933
- Blyth S. et al., 2016, Proc. Sci. MeerKAT Science: On the Pathway to the SKA. SISSA, Trieste, PoS#4
- Bok J., Blyth S. L., Gilbank D. G., Elson E. C., 2019, *MNRAS*, 484, 582
- Chung A., van Gorkom J. H., Kenney J. D. P., Crowl H., Vollmer B., 2009, *AJ*, 138, 1741
- Conselice C. J., 1997, *PASP*, 109, 1251
- Conselice C. J., 2006, *MNRAS*, 373, 1389
- Conselice C. J., Bershady M. A., Jangren A., 2000, *ApJ*, 529, 886
- Conselice C. J., Bershady M. A., Dickinson M., Papovich C., 2003, *AJ*, 126, 1183
- Crain R. A. et al., 2015, *MNRAS*, 450, 1937
- Crain R. A. et al., 2017, *MNRAS*, 464, 4204
- Dalla Vecchia C., Schaye J., 2012, *MNRAS*, 426, 140
- de Jong R. S., 1996a, *A&AS*, 118, 557
- de Jong R. S., 1996b, *A&A*, 313, 45
- de Vaucouleurs G., 1948, *Ann. Astrophys.*, 11, 247
- de Vaucouleurs G., 1959, *Handbuch Phys.*, 53, 275
- Deg N., Blyth S. L., Hank N., Kruger S., Carignan C., 2020, *MNRAS*, 495, 1984
- Dolag K., Borgani S., Murante G., Springel V., 2009, *MNRAS*, 399, 497
- Dressler A., 1980, *ApJ*, 236, 351
- Dressler A., 1984, *ARA&A*, 22, 185
- Elmegreen D. M., Elmegreen B. G., 1987, *ApJ*, 314, 3
- Espada D., Verdes-Montenegro L., Huchtmeier W. K., Sulentic J., Verley S., Leon S., Sabater J., 2011, *A&A*, 532, A117
- Fernández X. et al., 2013, *ApJ*, 770, L29
- Giese N., van der Hulst T., Serra P., Oosterloo T., 2016, *MNRAS*, 461, 1656
- Haardt F., Madau P., 2001, in Neumann D. M., Tran J. T. V., eds, XXXVIth Rencontres de Moriond, XXIst Moriond Astrophysics Meeting, March 10-17, 2001 Savoie, France: Clusters of Galaxies and the High Redshift Universe Observed in X-rays. p. 64
- Haynes M. P., Hogg D. E., Maddalena R. J., Roberts M. S., van Zee L., 1998, *AJ*, 115, 62
- Heald G. et al., 2011, *A&A*, 526, A118
- Hibbard J. E., van Gorkom J. H., Rupen M. P., Schiminovich D., 2001, in Hibbard J. E., Rupen M., van Gorkom J. H., eds, ASP Conf. Ser. Vol. 240, Gas and Galaxy Evolution. Astron. Soc. Pac., San Francisco, p. 657
- Holmberg E., 1958, *Medd. fran Lunds Astron. Obs. Ser. II*, 136, 1
- Holwerda B. W., Pirzkal N., de Blok W. J. G., Bouchard A., Blyth S.-L., van der Heyden K. J., Elson E. C., 2011, *MNRAS*, 416, 2415
- Hubble E. P., 1926, *ApJ*, 64, 321
- Jarvis M. et al., 2016, Proc. Sci. MeerKAT Science: On the Pathway to the SKA. SISSA, Trieste, PoS#6
- Koribalski B. S. et al., 2020, *Ap&SS*, 365, 118
- Kormendy J., 1977a, *ApJ*, 217, 406
- Kormendy J., 1977b, *ApJ*, 218, 333
- Kormendy J., 1979, *ApJ*, 227, 714
- Kormendy J., 2009, in Jogee S., Marinova I., Hao L., Blanc G. A., eds, ASP Conf. Ser. Vol. 419, Galaxy Evolution: Emerging Insights and Future Challenges. Astron. Soc. Pac., San Francisco, p. 87
- Lelli F., Verheijen M., Fraternali F., 2014, *MNRAS*, 445, 1694
- Lotz J. M., Primack J., Madau P., 2004, *AJ*, 128, 163
- McAlpine S. et al., 2016, *Astron. Comput.*, 15, 72
- Marasco A., Crain R. A., Schaye J., Bahé Y. M., van der Hulst T., Theuns T., Bower R. G., 2016, *MNRAS*, 461, 2630
- Moore B., Lake G., Katz N., 1998, *ApJ*, 495, 139
- Oman K. A., 2019, Astrophysics Source Code Library, record ascl:1911.005
- Oman K. A., Marasco A., Navarro J. F., Frenk C. S., Schaye J., Benítez-Llambay A., 2019, *MNRAS*, 482, 821
- Planck Collaboration I, 2014, *A&A*, 571, A1
- Rahmati A., Pawlik A. H., Raičević M., Schaye J., 2013, *MNRAS*, 430, 2427
- Reynolds T. N., Westmeier T., Staveley-Smith L., Chauhan G., Lagos C. D. P., 2020, *MNRAS*, 493, 5089
- Richter O.-G., Sancisi R., 1994, *A&A*, 290, L9
- Roberts M. S., Haynes M. P., 1994, *ARA&A*, 32, 115
- Rosas-Guevara Y. M. et al., 2015, *MNRAS*, 454, 1038
- Saintonge A., 2007, *AJ*, 133, 2087
- Sancisi R., 1999, in Barnes J. E., Sanders D. B., eds, Proceedings of IAU Symposium #186: Galaxy Interactions at Low and High Redshift, Kyoto, Japan, 26-30 August, 1997. p. 71
- Sancisi R., Fraternali F., Oosterloo T., van der Hulst T., 2008, *A&AR*, 15, 189
- Sandage A., 1961, The Hubble Atlas of Galaxies. Carnegie Institution, Washington
- Schade D., Lilly S. J., Crampton D., Hammer F., Le Fevre O., Tresse L., 1995, *ApJ*, 451, L1
- Schaye J., Dalla Vecchia C., 2008, *MNRAS*, 383, 1210
- Schaye J. et al., 2015, *MNRAS*, 446, 521
- Scott T. C., Brinks E., Cortese L., Boselli A., Bravo-Alfaro H., 2018, *MNRAS*, 475, 4648
- Sérsic J. L., 1963, *Bol. Asoc. Argentina Astron. La Plata Argentina*, 6, 41
- Springel V., 2005, *MNRAS*, 364, 1105
- Swaters R. A., Schoenmakers R. H. M., Sancisi R., van Albada T. S., 1999, *MNRAS*, 304, 330
- Verheijen M. A. W., Sancisi R., 2001, *A&A*, 370, 765
- Verheijen M. A. W., Zwaan M., 2001, in Hibbard J. E., Rupen M., van Gorkom J. H., eds, ASP Conf. Ser. Vol. 240, Gas and Galaxy Evolution. Astron. Soc. Pac., San Francisco, p. 867
- Warmels R. H., 1988, *A&AS*, 72, 57
- Watts A. B., Catinella B., Cortese L., Power C., 2020, *MNRAS*, 492, 3672
- Wendland H., 1995, *Adv. Comput. Math.*, 4, 389
- Wiersma R. P. C., Schaye J., Smith B. D., 2009a, *MNRAS*, 393, 99
- Wiersma R. P. C., Schaye J., Theuns T., Dalla Vecchia C., Tornatore L., 2009b, *MNRAS*, 399, 574
- Yu N., Ho L. C., Wang J., 2020, *ApJ*, 898, 102
- van Eymeren J., Jütte E., Jog C. J., Stein Y., Dettmar R. J., 2011, *A&A*, 530, A30
- van den Bergh S., 1960, *ApJ*, 131, 215
- van den Bergh S., 1976, *ApJ*, 206, 883
- van der Hulst J. M., van Albada T. S., Sancisi R., 2001, in Hibbard J. E., Rupen M., van Gorkom J. H., eds, ASP Conf. Ser. Vol. 240, Gas and Galaxy Evolution. Astron. Soc. Pac., San Francisco, p. 451

SUPPORTING INFORMATION

Supplementary data are available at [MNRAS](https://www.mnras.org/) online.

Table S1. Properties of the mock sample of galaxies extracted from the Eagle simulations.

Please note: Oxford University Press is not responsible for the content or functionality of any supporting materials supplied by the authors. Any queries (other than missing material) should be directed to the corresponding author for the article.

APPENDIX A: PROPERTIES OF MOCK GALAXIES

In Table A1, we present the group numbers of mock galaxies from the Recal25 run of the EAGLE simulations and properties derived from the mock datacubes for each galaxy. We select central galaxies from each FoF group at $z = 0$ with maximum rotational velocities (V_{\max}) in the range $80 \text{ km s}^{-1} < V_{\max} < 200 \text{ km s}^{-1}$. Thus, each galaxy mentioned in this table has SubGroupNumber = 0 and SnapNum = 28 in the SubHalo table of Recal25 in the EAGLE data base (see <http://icc.dur.ac.uk/Eagle/database.php> and McAlpine et al. 2016). The full table is available as supplementary online material.

APPENDIX B: ATLAS PAGES OF MOCK GALAXIES

Fig B1 shows an example atlas page, where each page has data products of three mock galaxies. For each galaxy, we present noise-free H I data products derived in Section 3.2. The FoF group number of the galaxy, its maximum rotational velocity and logarithm of H I mass is shown above each row. We present column density maps at angular resolutions of 12×17 , 30, 45, 56, and 98 arcsec in which column densities of 1, 5, and $15 \times 10^{19} \text{ cm}^{-2}$ are shown as red, blue, and green contours, respectively. Each panel showing column density maps is 100 kpc across. At each angular resolution, the A_{mod} value measured at a column density threshold of $5 \times 10^{19} \text{ cm}^{-2}$ is shown in the top right corner. The centre around which the galaxy is rotated is shown with a yellow cross. A noise-free global profile of the galaxy derived at 56 arcsec is shown, where blue dashed lines indicate velocities at 20 per cent of the peak flux and the green dashed line indicates the systemic velocity. The A_{flux} of the galaxy is shown in the top right corner. The atlas pages are available in full as supplementary online material.

Table A1. Properties of the mock sample of galaxies extracted from the EAGLE simulations. Columns: (1) GroupNumber of the central galaxy; (2) Maximum rotational velocity; (3) H I mass; (4) Inclination; (5) to (9) A_{mod} value measured in noise-free column density maps with a threshold of $5 \times 10^{19} \text{ cm}^{-2}$ at resolutions of 12 arcsec \times 17 arcsec, 30, 45, 56, and 98 arcsec respectively; (10) A_{flux} value measured in 56 arcsec noise-free global profiles. Only a few rows are shown here, the full table can be found as supplementary online material.

| Group Number (Recal25_) | V_{\max} (km s^{-1}) | $\log(M_{\text{H I}})$ (M_{\odot}) | Inclination ($^{\circ}$) | $A_{\text{mod}}^{\text{nf}}$ (@12 arcsec) | $A_{\text{mod}}^{\text{nf}}$ (@30 arcsec) | $A_{\text{mod}}^{\text{nf}}$ (@45 arcsec) | $A_{\text{mod}}^{\text{nf}}$ (@56 arcsec) | $A_{\text{mod}}^{\text{nf}}$ (@98 arcsec) | $A_{\text{flux}}^{\text{nf}}$ (@56 arcsec) |
|----------------------------|--------------------------------------|-------------------------------------------|-------------------------------|----------------------------------------------|----------------------------------------------|----------------------------------------------|----------------------------------------------|----------------------------------------------|-----------------------------------------------|
| 17 | 205 | 9.98 | 49 | 0.82 | 0.77 | 0.72 | 0.68 | 0.49 | 1.18 |
| 25 | 199 | 9.98 | 65 | 0.90 | 0.89 | 0.86 | 0.84 | 0.77 | 1.35 |
| 27 | 185 | 9.53 | 66 | 0.95 | 0.93 | 0.90 | 0.86 | 0.50 | 1.26 |
| 28 | 198 | 9.86 | 93 | 0.84 | 0.81 | 0.77 | 0.74 | 0.54 | 1.20 |
| 30 | 193 | 9.22 | 108 | 0.88 | 0.83 | 0.78 | 0.73 | 0.60 | 1.04 |
| 31 | 189 | 10.00 | 65 | 0.73 | 0.69 | 0.65 | 0.61 | 0.53 | 1.10 |
| 32 | 183 | 9.96 | 41 | 0.90 | 0.89 | 0.89 | 0.88 | 0.85 | 1.19 |
| 33 | 166 | 10.25 | 83 | 0.77 | 0.75 | 0.74 | 0.73 | 0.69 | 1.24 |
| 34 | 174 | 10.10 | 111 | 0.74 | 0.71 | 0.67 | 0.64 | 0.55 | 1.10 |
| 35 | 178 | 9.76 | 19 | 0.65 | 0.59 | 0.52 | 0.48 | 0.37 | 1.15 |
| 36 | 180 | 9.42 | 75 | 0.48 | 0.42 | 0.37 | 0.35 | 0.29 | 1.02 |
| 37 | 158 | 9.87 | 17 | 0.85 | 0.83 | 0.81 | 0.80 | 0.74 | 1.12 |
| 38 | 167 | 9.81 | 115 | 0.63 | 0.58 | 0.53 | 0.50 | 0.43 | 1.08 |
| 39 | 141 | 9.85 | 73 | 0.77 | 0.75 | 0.73 | 0.71 | 0.67 | 1.03 |
| 40 | 166 | 9.95 | 44 | 0.73 | 0.70 | 0.67 | 0.64 | 0.56 | 1.17 |

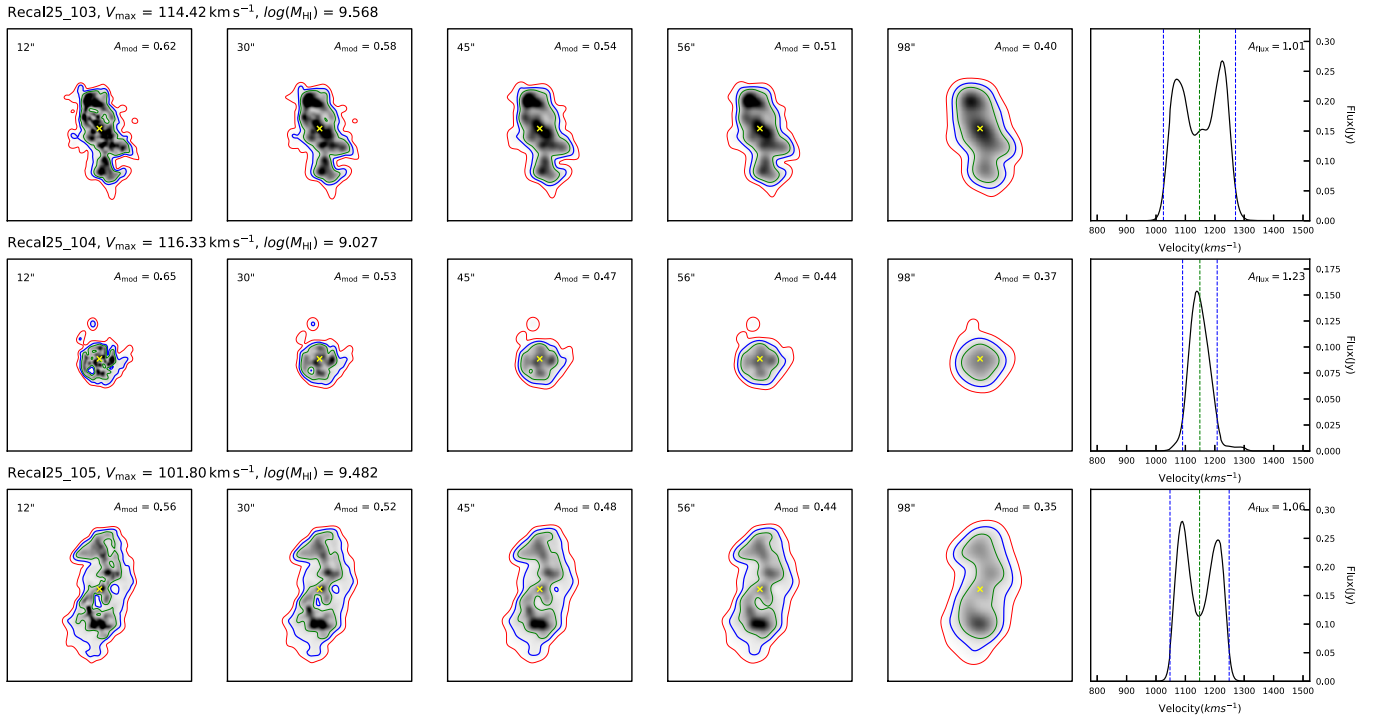


Figure B1. An example of atlas page, see text of Appendix B for detail.

This paper has been typeset from a $\text{T}_{\text{E}}\text{X}/\text{L}_{\text{A}}\text{T}_{\text{E}}\text{X}$ file prepared by the author.